Supporting Information

Dynamic regulation of ion transport through a bis(1,3-propanediol)-based channel via allosteric azobenzene photoswitching

Manzoor Ahmad,[a,c] Susmita Sarkar,[b] Ravi Bogade,[a] Abhishek Mondal,[a,d] Debashis Mondal,[a,e] Jagannath Mondal,[b] and Pinaki Talukdar[a]*

[a] *Department of Chemistry, Indian Institute of Science Education and Research Pune, Dr. Homi Bhabha Road, Pashan, Pune 411008, Maharashtra, India.*

[b] *Center for Interdisciplinary Sciences, Tata Institute of Fundamental Research, Hyderabad 500046, Telangana, India*

[c] *Present Address: Chemistry Research Laboratory, Mansfield Road, Oxford, OX1 3TA, UK*

[d] *Leiden Institute of Chemistry, Leiden University Einsteinweg 55, 2333 CC Leiden (The Netherlands)*

[e] *Present Address: Faculty of Chemistry, Biological and Chemical Research Centre, University of Warsaw, Zwirkii Wigury 101, Warsaw 02-089, Poland*

*To whom correspondence should be addressed. Email: ptalukdar@iiserpune.ac.in

Table of contents

I. General Methods

All chemical reactions were performed under the nitrogen atmosphere. All reagents and solvents for synthesis were purchased from commercial sources (Sigma-Aldrich, Spectrochem) and used further without purification. The column chromatography was carried out using Merck silica (100-200/ 230-400 mesh size). The thin layer chromatography was performed on E. Merck silica gel 60-F254 plates. Egg yolk phosphatidylcholine (EYPC) as a solution of chloroform (25 mg/mL), mini extruder, and polycarbonate membrane of 100 nm and 200 nm were purchased from Avanti Polar Lipid. HEPES, HPTS, lucigenin, NaOH, Triton X-100, FCCP, valinomycin, and all inorganic salts were obtained as molecular biology grade from Sigma Aldrich.

II. Physical Measurements

The ^{1}H NMR spectra were recorded at 400 MHz, whereas ^{13}C spectra were at 101 MHz. The residual solvent signals were considered as an internal reference (δ_H = 7.26 ppm for $CDCl_3$, δ_H = 2.50 for DMSO-d_6, and δ_H = 1.94 for CD_3CN) to calibrate spectra. The chemical shifts were reported in ppm. The following abbreviations were used to indicate multiplicity patterns: m: multiplet, s: singlet, d: doublet, t: triplet, dd: doublet of doublets, dq: doublet of quartets, ddd: doublet of doublet of doublets, p: pentet. Coupling constants were measured in Hz. Infra-red (IR) spectra were measured in cm^{-1} using an FT–IR spectrophotometer. Melting points were measured on a micro melting point apparatus. High-resolution mass spectra (HRMS) were recorded on electrospray ionization time-of-flight (ESI-TOF). Fluorescence experiments were recorded on Fluoromax-4 from Jobin Yvon Edison, equipped with an injector port and magnetic stirrer in a microfluorescence cuvette. All buffer solutions were prepared from the autoclaved water. Adjustment of the pH of buffer solutions was made using a Helmer pH meter. The extravesicular dye was removed by performing gel chromatography using Sephadex. The fluorescence studies were processed using OriginPro 8.5. ChemBio Draw 15 Ultra software was used to draw structures and process Fig.s. UV-vis spectra were recorded on a Varian Cary 5000 spectrophotometer.

III. Synthesis

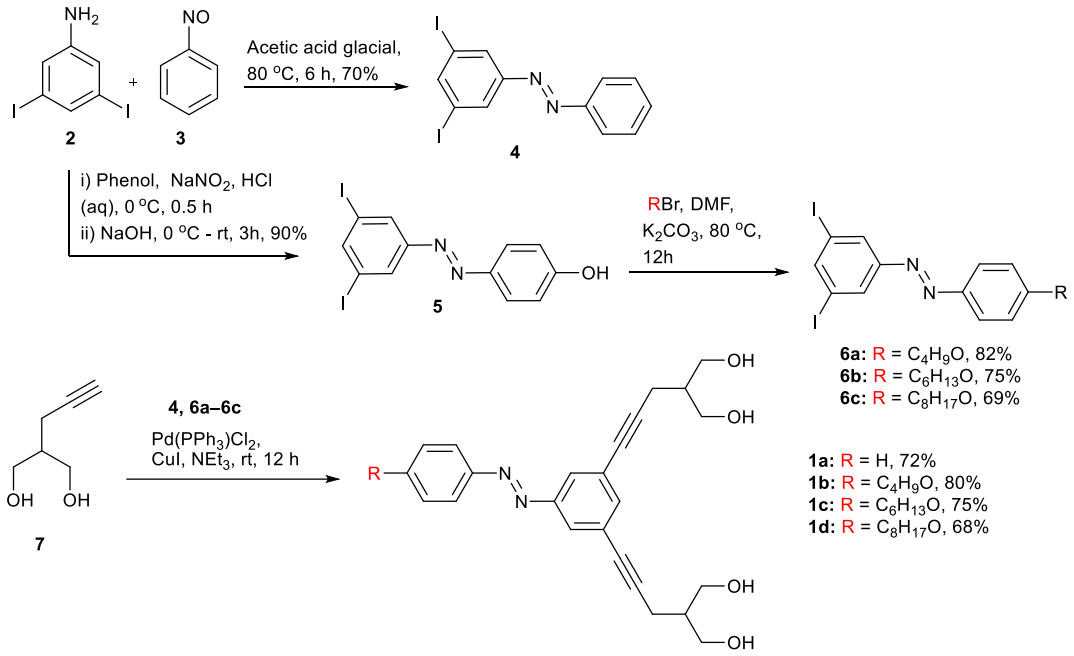

Scheme 1: Synthesis of the desired compounds **1a-1d**.

(*E*)-1-(3,5-diiodophenyl)-2-phenyldiazene ($C_{12}H_8I_2N_2$) (4): In a 50 mL round bottom flask,

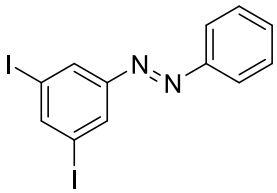

nitrosobenzene **3** (62 mg, 0.6 mmol, 1.0 equiv) and 3,5-diiodoaniline **2** (200 mg, 0.6 mmol, 1.0 equiv) were dissolved in 10 mL of glacial acetic acid and heated at reflux. After 6 h, the mixture was cooled to room temperature, and the crude mixture was then extracted with dichloromethane (3 × 30 mL). The organic layer was dried with anhydrous sodium sulfate, filtered, and concentrated under reduced pressure to give the crude product. The residue was then purified by column chromatography over 100–200 mesh silica gel (*Eluent*: EtOAc : petroleum ether 1:9 v/v) to furnish **4** as yellow solid (175 mg, 70%). **^{1}H NMR (400 MHz, Chloroform-*d*):** δ 8.22 (d, *J* = 1.6 Hz, 2H), 8.14 (t, *J* = 1.6 Hz, 1H), 7.93–7.88 (m, 2H), 7.56–7.51 (m, 3H); **^{13}C NMR (101 MHz, Chloroform-*d*):** δ 146.9, 132.1, 131.5, 129.4, 123.3, 95.0, 77.2; **IR (Neat, ν/cm^{-1}):** 3056, 2920, 2851, 1589, 1495, 1451, 1241; **HRMS (ESI):** Calc. for $C_{16}H_{15}N_3O_3H^+$ $[M+H]^+$: 434.8849, found 434.8858.

(*E*)-4-((3,5-diiodophenyl)diazenyl)phenol ($C_{12}H_8I_2N_2O$) (5): In a 50 mL round bottom flask,

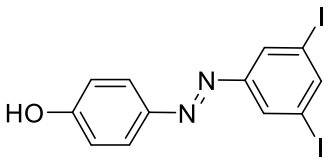

3,5-diiodoaniline **2** (1.00 g, 2.9 mmol, 1 equiv) was added to 37% HCl (aq) solution (15 mL) at 0 °C. To this solution, $NaNO_2$ (260 mg, 3.77 mmol, 1.3 equiv) in 10 mL of water was added dropwise. After mixing, the resulting solution was stirred for 40 min at 0 °C

to form a diazo salt solution. Then, a separate solution was prepared using phenol (272 mg, 2.9 mmol, 1 equiv) and 1.00 g of NaOH in 10 mL of water. The diazo salt solution was slowly added to this phenol solution under an ice water bath. The color of the solution would become dark during this process. After stirring at 0 °C for 1 h, the resulting solution was acidified by adding 20% HCl (aq) solution. Afterwards, the crude mixture was then extracted with dichloromethane (3 × 30 mL). The organic layer was dried with anhydrous sodium sulfate, filtered, and concentrated under reduced pressure to give the crude product. The residue was then purified by column chromatography over 100–200 mesh silica gel (*Eluent*: EtOAc : petroleum ether 3:7 v/v) to furnish **5** as red solid (1.13 g, 90%). **^{1}H NMR (400 MHz, DMSO-*d*$_6$):** δ 8.16 (d, *J* = 1.5 Hz, 2H), 8.09 (t, *J* = 1.5 Hz, 1H), 7.86 (d, *J* = 8.9 Hz, 2H), 6.95 (d, *J* = 8.9 Hz, 2H), 5.54 (s, 1H); **^{13}C NMR (101 MHz, DMSO-*d*$_6$):** δ 159.3, 146.8, 146.3, 131.2, 125.7, 116.1, 94.9, 77.1; **IR (Neat, ν/cm^{-1}):** 3347 (broad signal), 2161, 1639, 1212, 855, 769; **HRMS (ESI):** Calc. for $C_{16}H_{15}N_3O_3H^+$ $[M+H]^+$: 450.8798, found 450.8809.

General procedure for the synthesis of compounds 6a–6c

In a 25 mL oven-dried round bottom flask, compound **5** (200 mg, 1 equiv) and K_2CO_3 (2 equiv) were added and heated for 30 min at 50 °C in an oil bath. After that, an appropriate alkyl bromide (1 equiv) was added to the reaction mixture, and the reaction was refluxed for 12 h. After the completion of the reaction, monitored through TLC, the excess of the solvent was removed under reduced pressure through a rotary evaporator. The crude mixture was then extracted with dichloromethane (3 × 30 mL). The organic layer was dried with anhydrous sodium sulfate, filtered, and concentrated under reduced pressure to give the crude product. The residue was then purified by column chromatography over 100–200 mesh silica gel to afford the desired compounds **6a–6c** in 69–82% yield.

(*E*)-1-(4-butoxyphenyl)-2-(3,5-diiodophenyl)diazene ($C_{16}H_{16}I_2N_2O$) (6a): Synthesized by

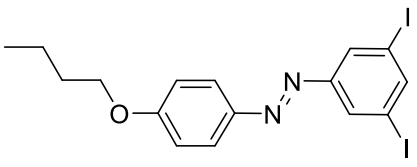

reacting (*E*)-4-((3,5-diiodophenyl)diazenyl)phenol **5** (200 mg, 0.4 mmol, 1 equiv) with bromobutane (120 mg, 0.8 mmol, 2 equiv). The crude product was purified by column chromatography over 100–200 mesh silica gel (*Eluent*: EtOAc : petroleum ether 2:8 v/v) to furnish **6a** as red solid (183 mg, 82%). **^{1}H NMR (400 MHz, DMSO-*d*$_6$):** δ 8.16 (d, *J* = 1.5 Hz, 2H), 8.08 (t, *J* = 1.5 Hz, 1H), 7.88 (d, *J* = 9.0 Hz, 2H), 7.00 (d, *J* = 9.0 Hz, 2H), 4.06 (t, *J* = 6.5 Hz, 2H), 1.85–1.77 (m, 2H), 1.55–1.48 (m, 2H), 1.00 (t, *J* = 7.4 Hz, 3H); **^{13}C NMR (101 MHz, DMSO-*d*$_6$):** δ 162.5, 153.9, 146.4, 145.9, 131.0,

125.3, 114.8, 94.8, 68.1, 31.2, 19.2, 13.8; **IR (Neat, ν/cm^{-1}):** 3066, 2924, 2857, 1592, 1498, 1460, 1398, 1307, 1242; **HRMS (ESI):** Calc. for $C_{16}H_{15}N_3O_3H^+$ $[M+H]^+$: 506.9424, found 506.9430.

(*E*)-1-(3,5-diiodophenyl)-2-(4-(hexyloxy)phenyl)diazene ($C_{18}H_{20}I_2N_2O$) (6b): Synthesized

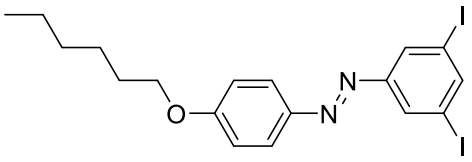

by reacting (*E*)-1-(3,5-diiodophenyl)-2-(4-(hexyloxy)phenyl)diazene **5** (200 mg, 0.4 mmol, 1 equiv) with bromohexane (73 mg, 0.4 mmol, 1 equiv). The crude product was purified by column chromatography over 100–200 mesh silica gel (*Eluent*: EtOAc : petroleum ether 1:9 v/v) to furnish **6b** as red solid (177 mg, 75%). **^{1}H NMR (400 MHz, DMSO-*d*$_6$):** δ 8.17 (d, *J* = 1.6 Hz, 2H), 8.08 (t, *J* = 1.5 Hz, 1H), 7.89 (d, *J* = 9.0 Hz, 2H), 7.00 (d, *J* = 9.0 Hz, 2H), 4.05 (t, *J* = 6.6 Hz, 2H), 1.85–1.79 (m, 2H), 1.51–1.46 (m, 2H), 1.36 (ddd, *J* = 7.2, 3.4, 1.1 Hz, 4H), 0.94–0.90 (m, 3H); **^{13}C NMR (101 MHz, DMSO-*d*$_6$):** δ 162.5, 146.4, 146.0, 131.0, 125.3, 114.8, 94.8, 68.5, 31.6, 29.1, 25.7, 22.6, 14.0; **IR (Neat, ν/cm^{-1}):** 3070, 2926, 2857, 1592, 1498, 1465, 1398, 1307, 1244; **HRMS (ESI):** Calc. for $C_{16}H_{15}N_3O_3H^+$ $[M+H]^+$: 534.9737, found 534.9750.

(*E*)-1-(3,5-diiodophenyl)-2-(4-(octyloxy)phenyl)diazene ($C_{20}H_{24}I_2N_2O$) (6c): Synthesized

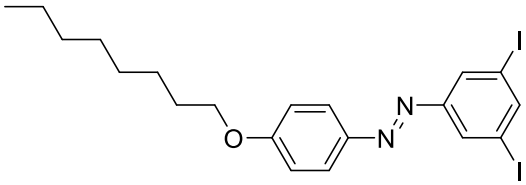

by reacting (*E*)-1-(3,5-diiodophenyl)-2-(4-(octyloxy)phenyl)diazene **5** (200 mg, 0.4 mmol, 1 equiv) with bromooctane (85 mg, 0.4 mmol, 1 equiv). The crude product was purified by column chromatography over 100–200 mesh silica gel (*Eluent*: EtOAc : petroleum ether 1:9 v/v) to furnish **6c** as red solid (171 mg, 69%). **^{1}H NMR (400 MHz, DMSO-*d*$_6$):** δ 8.16 (d, *J* = 1.5 Hz, 2H), 8.08 (t, *J* = 1.5 Hz, 1H), 7.90–7.87 (m, 2H), 7.02–6.97 (m, 2H), 4.04 (t, *J* = 6.6 Hz, 2H), 1.86–1.79 (m, 2H), 1.52–1.45 (m, 2H), 1.34–1.28 (m, 8H), 0.90 (s, 3H); **^{13}C NMR (101 MHz, DMSO-*d*$_6$):** δ 162.5, 146.4, 145.9, 131.1, 125.3, 114.8, 94.8, 68.5, 31.8, 29.3, 29.2, 29.2, 26.0, 22.7, 14.1; **IR (Neat, ν/cm^{-1}):** 3065, 2926, 2860, 1592, 1498, 1468, 1398, 1307, 1250; **HRMS (ESI):** Calc. for $C_{16}H_{15}N_3O_3H^+$ $[M+H]^+$: 563.0050, found 56.0061.

General procedure for the synthesis of compounds 1a–1d: In a 25 mL oven-dried round bottom flask, a solution of diiodo azobenzene derivatives **4**, **6a–6c** (100 mg, 1 equiv), CuI (0.04 equiv) and $Pd(PPh_3)_2Cl_2$ (0.02 equiv) in Et_3N (5 mL) was added 2-(prop-2-yn-1-yl)propane-1,3-diol **7** (3 equiv). Then, the resulting mixture was heated under a nitrogen atmosphere at 60 °C for 12 h. The reaction was monitored by TLC to establish the consumption of starting

material. After the mixture was cooled to room temperature, the crude mixture was then extracted with dichloromethane (3 × 30 mL). The organic layer was dried with anhydrous sodium sulfate, filtered, and concentrated under reduced pressure to give the crude product. The residue was then purified by column chromatography over 100–200 mesh silica gel to afford the desired compounds **1a–1d** in 68–80% yield.

(*E*)-2,2'-((5-(phenyldiazenyl)-1,3-phenylene)bis(prop-2-yne-3,1-diyl))bis(propane-1,3-diol) ($C_{24}H_{26}N_2O_4$) (1a): Synthesized by reacting (*E*)-1-(3,5-diiodophenyl)-2-phenyldiazene **4** (100 mg, 0.2 mmol, 1 equiv) with 2-(prop-2-yn-1-yl)propane-1,3-diol **7** (78 mg, 0.7 mmol, 3 equiv). The crude product was purified by column chromatography over 100–200 mesh silica gel (*Eluent*: 5% methanol in chloroform) to furnish **1a** as reddish oily liquid as *E*:*Z* mixture in a ratio of 95:5 (67 mg, 72%). **^{1}H NMR (400 MHz, DMSO-*d*6) of 1a-*E*:** δ 7.94–7.91 (m, 2H), 7.79 (d, *J* = 1.6 Hz, 2H), 7.64–7.60 (m, 3H), 7.54 (t, *J* = 1.5 Hz, 1H), 4.55 (t, *J* = 5.2 Hz, 4H), 3.54–3.44 (m, 8H), 1.80 (p, *J* = 6.2 Hz, 2H); **^{13}C NMR (101 MHz, DMSO-*d*$_6$) of 1a-*E*:** δ 135.9, 132.2, 129.5, 124.9, 124.3, 122.8, 91.6, 79.4, 60.7, 43.2, 39.5, 17.8; **IR (Neat, ν/cm^{-1}):** 3348 (broad signal), 2926, 1644, 1594, 1502, 1464, 1304, 1248; **HRMS (ESI):** Calc. for $C_{16}H_{15}N_3O_3H^+$ $[M+H]^+$: 407.1965, found 407.1960.

(*E*)-2,2'-((5-((4-butoxyphenyl)diazenyl)-1,3-phenylene)bis(prop-2-yne-3,1-diyl))bis(propane-1,3-diol) ($C_{28}H_{34}N_2O_5$) (1b): Synthesized by reacting (*E*)-1-(4-butoxyphenyl)-2-(3,5-diiodophenyl)diazene **6a** (100 mg, 0.2 mmol, 1 equiv) with 2-(prop-2-yn-1-yl)propane-1,3-diol **7** (67 mg, 0.7 mmol, 3 equiv) with The crude product was purified by column chromatography over 100–200 mesh silica gel (*Eluent*: 5% methanol in chloroform) to furnish **1b** as reddish oily liquid as *E*:*Z* mixture in a ratio of 78:22 (75 mg, 80%). **^{1}H NMR (400 MHz, DMSO-*d*$_6$) of 1b-*E*:** δ 7.92–7.88 (m, 2H), 7.73 (d, *J* = 1.5 Hz, 2H), 7.48 (t, *J* = 1.5 Hz, 1H), 7.14 (d, *J* = 9.1 Hz, 2H), 6.78 (d, *J* = 1.5 Hz, 0H), 6.71 (s, 0H), 4.54 (t, *J* = 5.2 Hz, 4H), 4.10 (t, *J* = 6.5 Hz, 2H), 3.53–3.45 (m, 8H), 1.84–1.77 (m, 2H), 1.76–1.71 (m, 2H), 1.50–

1.43 (m, 2H), 0.96 (d, *J* = 7.3 Hz, 3H); **^{13}C NMR (101 MHz, DMSO-*d*$_6$) of 1b-*E*:** δ 167.3, 157.2, 151.1, 130.2, 130.1, 129.3, 120.3, 96.6, 84.8, 73.0, 65.9, 48.4, 35.8, 34.2, 23.9, 23.0, 18.9; **IR (Neat, ν/cm^{-1}):** 3350 (broad signal), 2928, 1644, 1599, 1506, 1464, 1304, 1242; **HRMS (ESI):** Calc. for $C_{16}H_{15}N_3O_3H^+$ $[M+H]^+$: 479.2540, found 479.2542.

(*E*)-2,2'-((5-((4-(hexyloxy)phenyl)diazenyl)-1,3-phenylene)bis(prop-2-yne-3,1-diyl))bis(propane-1,3-diol) ($C_{30}H_{38}N_2O_5$) (**1c**) Synthesized by reacting (*E*)-1-(3,5-diiodophenyl)-2-(4-(hexyloxy) phenyl) diazene **6b** (100 mg, 0.2 mmol, 1 equiv) with 2-(prop-2-yn-1-yl)propane-1,3-diol **7** (64 mg, 0.7 mmol, 3 equiv). The crude product was purified by column chromatography over 100–200 mesh silica gel (*Eluent*: 5% methanol in chloroform) to furnish **1c** as reddish oily liquid as *E*:*Z* mixture in a ratio of 88:12 (70 mg, 75%). **^{1}H NMR (400 MHz, DMSO-*d*$_6$) of 1c-*E*:** δ 7.94–7.87 (m, 2H), 7.73 (d, *J* = 1.5 Hz, 2H), 7.48 (t, *J* = 1.5 Hz, 1H), 7.13 (d, *J* = 9.1 Hz, 2H), 4.54 (t, *J* = 5.2 Hz, 4H), 4.09 (t, *J* = 6.5 Hz, 2H), 3.49 (dq, *J* = 16.8, 5.2 Hz, 8H), 1.84–1.77 (m, 2H), 1.77–1.71 (m, 2H), 1.47–1.39 (m, 2H), 1.34–1.29 (m, 4H), 0.90–0.86 (m, 3H); **^{13}C NMR (101 MHz, DMSO-*d*$_6$) of 1c-*E*:** δ 152.5, 146.3, 125.5, 125.3, 124.5, 115.6, 91.8, 80.0, 68.5, 61.2, 43.6, 31.4, 28.9, 25.6, 22.5, 18.2, 14.4; **IR (Neat, ν/cm^{-1}):** 3400 (broad signal), 2930, 1645, 1591, 1506, 1462, 1304, 1248; **HRMS (ESI):** Calc. for $C_{16}H_{15}N_3O_3H^+$ $[M+H]^+$: 507.2853, found 507.2859.

(*E*)-2,2'-((5-((4-(octyloxy)phenyl)diazenyl)-1,3-phenylene)bis(prop-2-yne-3,1-diyl))bis(propane-1,3-diol) ($C_{32}H_{42}N_2O_5$) (1d): Synthesized by reacting (*E*)-1-(3,5-diiodophenyl)-2-(4-(octyloxy) phenyl) diazene **6c** (100 mg, 0.2 mmol, 1 equiv) with 2-(prop-2-yn-1-yl)propane-1,3-diol **7** (60 mg, 0.7 mmol, 3 equiv). The crude product was purified by column chromatography over 100–200 mesh silica gel (*Eluent*: 5% methanol in chloroform) to furnish **1d** as reddish oily liquid as *E*:*Z* mixture in a ratio of 90:10 (64 mg, 68%). **^{1}H NMR (400 MHz, DMSO-*d*$_6$) of 1d-*E*:** δ 7.90

(d, *J* = 9.0 Hz, 2H), 7.73 (d, *J* = 1.5 Hz, 2H), 7.48 (s, 1H), 7.13 (d, *J* = 9.1 Hz, 2H), 4.54 (t, *J* = 5.2 Hz, 4H), 4.08 (t, *J* = 6.5 Hz, 2H), 3.54 – 3.46 (m, 8H), 1.78 (ddd, *J* = 25.7, 13.5, 7.0 Hz, 4H), 1.46–1.38 (m, 2H), 1.28 (dd, *J* = 12.7, 4.1 Hz, 8H), 0.87 (d, *J* = 6.7 Hz, 3H).); **^{13}C NMR (101 MHz, DMSO-d_6) of 1d-*E*:** 167.2, 157.2, 151.0, 140.4, 130.2, 130.0, 120.33, 96.6, 84.8, 73.3, 65.9, 48.4, 36.5, 33.9, 33.8, 33.7, 30.7, 27.3, 23.0, 19.2; **IR (Neat, ν/cm^{-1}):** 3402 (broad signal), 2925, 1641, 1588, 1500, 1462, 1301, 1241; **HRMS (ESI):** Calc. for $C_{16}H_{15}N_3O_3H^+$ $[M+H]^+$: 535.3166, found 535.3168.

IV. Ion Transport Studies [S1-S3]

Ion transporting activity studies across EYPC-LUVs⊃HPTS

Preparation of HEPES buffer and stock solutions: The HEPES buffer of pH = 7.0 was prepared by dissolving an appropriate amount of solid HEPES (10 mM) and NaCl (100 mM) in autoclaved water. The pH was adjusted to 7.0 by the addition of aliquots from 0.5 M NaOH solution. The stock solution of all carriers was prepared using HPLC grade DMSO.

Preparation of EYPC-LUVs⊃HPTS in NaCl: In a 10 mL clean and dry round bottom flask, a thin transparent film of egg yolk phosphatidylcholine (EYPC) was formed using a 1 mL EYPC lipid (25 mg/mL in $CHCl_3$) by providing continuous rotation and purging nitrogen gas. The transparent thin film was completely dried under a high vacuum for 4-5 h. After that, the transparent thin film was hydrated with 1 mL HEPES buffer (1 mM HPTS, 10 mM HEPES, 100 mM NaCl, pH = 7.0), and the resulting suspension was vortexed at 10 min intervals for 1 h. This hydrated suspension was subjected to 15 cycles of freeze-thaw (liquid N_2, 55 °C) followed by extrusion through 100 nm (pore size) polycarbonate membrane 21 times to obtain vesicles of an average 100 nm diameter. The extravesicular HPTS dyes were removed by size exclusion chromatography using Sephadex G-50 (Sigma-Aldrich) with eluting of HEPES buffer (10 mM HEPES, 100 mM NaCl, pH = 7.0). Finally, collected vesicles were diluted to 6 mL to get EYPC-LUVs⊃HPTS. *Final conditions:* ~ 5 mM EYPC, Inside: 1 mM HPTS, 10 mM HEPES, 100 mM NaCl, pH = 7.0, Outside: 10 mM HEPES, 100 mM NaCl, pH = 7.0.

Ion transport activity by HPTS assay: In clean and dry fluorescence cuvette, 1975 μL of HEPES buffer (10 mM HEPES, 100 mM NaCl, pH = 7.0) and 25 μL of EYPC–LUVs⊃HPTS vesicle was added. The cuvette was placed in a slowly stirring condition using a magnetic stirrer equipped with a fluorescence instrument (*t* = 0 s). The time-dependent HPTS emission intensity was monitored at λ_{em} = 510 nm (λ_{ex} = 450 nm) by creating a pH gradient between

intra- and extravesicular media by the addition of 0.5 M NaOH (20 μL) at $t = 20$ s. Then, different concentrations of transporter molecules in DMSO were added at $t = 100$ s. Finally, the vesicles were lysed by the addition of 10% Triton X-100 (25 μL) at $t = 300$ s to disturb the pH gradient.

The time axis was normalized according to Eq. S1:

$$t = t - 100 \qquad \text{Eq. S1}$$

The time-dependent data were normalized to percent change in fluorescence intensity using Eq. S2:

$$I_F = [(I_t - I_0) / (I_\infty - I_0)] \times 100 \qquad \text{Eq. S2}$$

where, I_0 is the initial intensity, I_t is the intensity at time t, and I_∞ is the final intensity after the addition of Triton X-100.

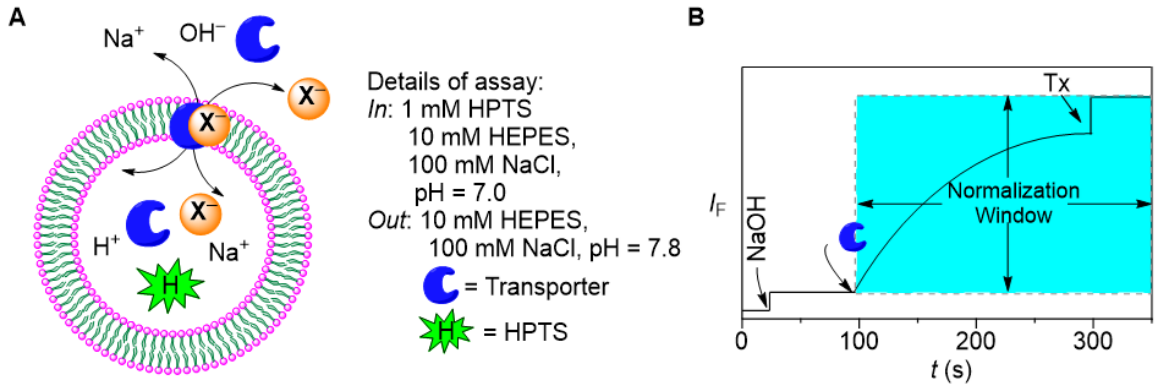

Fig. S1 Representations of fluorescence-based ion transport activity assay using EYPC-LUVs⊃HPTS (A), and illustration of ion transport kinetics showing normalization window (B).

Dose-response activity: The fluorescence kinetics of each transporter at different concentrations was studied. The concentration profile data were evaluated at $t = 290$ s to get effective concentration, EC_{50} (i.e. the concentration of transporter needed to achieve 50% chloride efflux)[S4] using the Hill Eq. (Eq. S3):

$$Y = Y_\infty + (Y_0 - Y_\infty) / [1 + (c/EC_{50})^n] \qquad \text{Eq. S3}$$

where, Y_0 = Fluorescence intensity just before the transporter addition (at t = 0 s), Y_∞ = Fluorescence intensity with excess transporter concentration, c = Concentration of transporter compound, and n = Hill coefficient (i.e., indicative for the number of monomers needed to form an active supramolecule).[5]

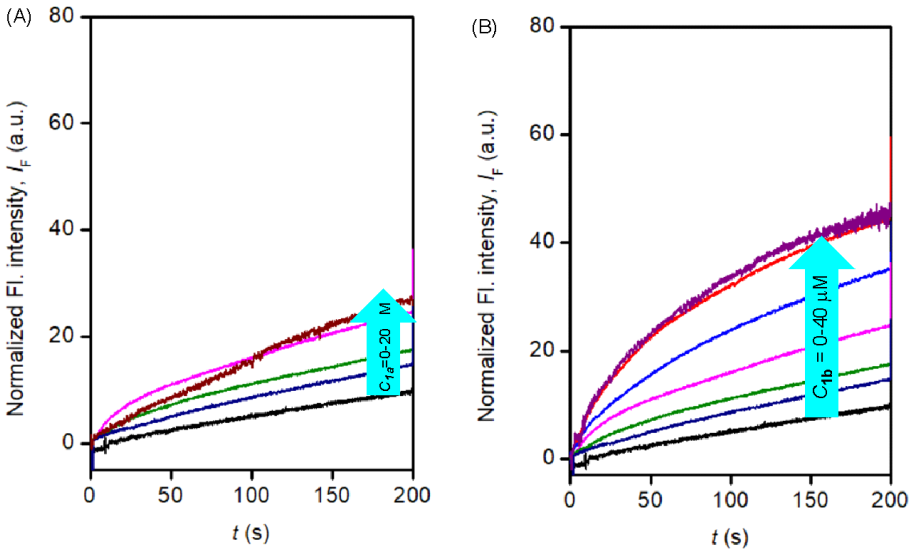

Fig. S2 Concentration-dependent activity of **1a** (A) and **1b** (B), respectively across EYPC-LUVs⊃HPTS.

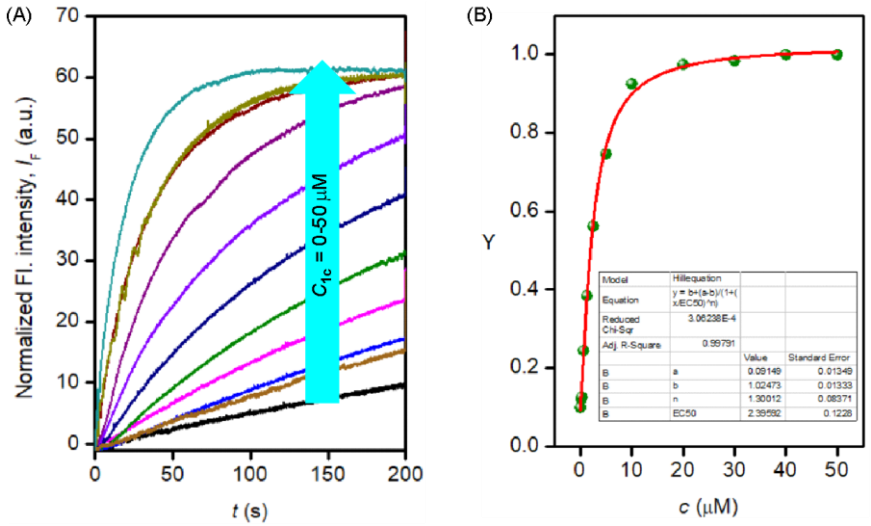

Fig. S3 Concentration-dependent activity of **1c** across EYPC-LUVs⊃HPTS (A). Dose-response plot of **1c** at 180 s after addition of compound (B).

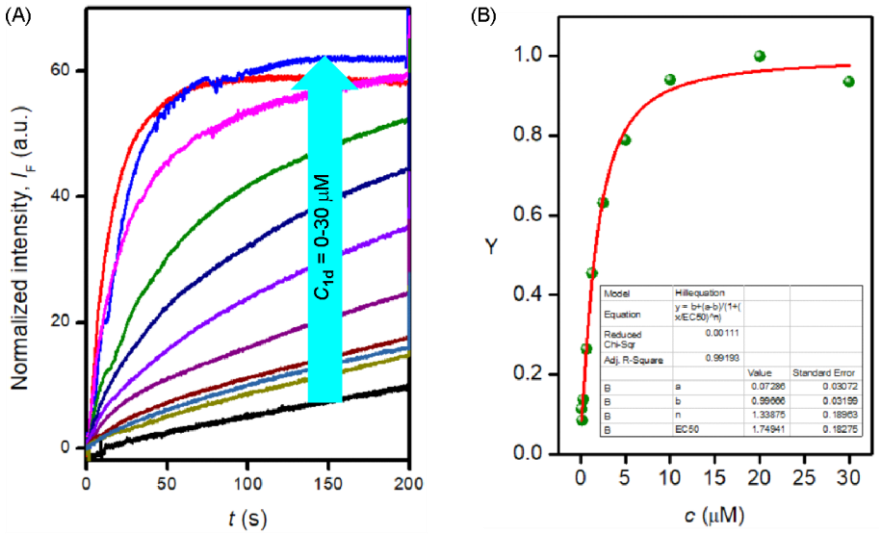

Fig. S4 Concentration-dependent activity of **1d** across EYPC-LUVs⊃HPTS (A). Dose-response plot of **1d** at 180 s after addition of compound (B).

Anion selectivity studies

Preparation of EYPC-LUVs⊃HPTS for anion selectivity: EYPC-LUVs⊃HPTS (~ 5.0 mM EYPC, inside: 1 mM HPTS, 10 mM HEPES, 100 mM NaCl, pH = 7.0 and outside: 10 mM HEPES, 100 mM NaX, pH = 7.0; where, X^- = Cl^-, Br^-, ClO_4^-, CN^-, NO_3^- and I^- were prepared following reported protocol.[S6]

Anion Selectivity Assay: In a clean fluorescence cuvette, 1975 μL of HEPES buffer (10 mM HEPES, 100 mM NaX, at pH = 7.0; where, X^- = Cl^-, Br^-, ClO_4^-, CN^-, NO_3^- and I^- was added followed by addition of 25 μL of EYPC-LUVs⊃HPTS vesicle in slowly stirring condition by a magnetic stirrer equipped with the fluorescence instrument (at t = 0 s). HPTS fluorescence emission intensity (F_t) was monitored with time at λ_{em} = 510 nm (λ_{ex} = 450 nm). 20 μL of 0.5 M NaOH was added to the cuvette at t = 20 s to make the pH gradient between the intra- and extravesicular system. The compound **1d** was added at t = 100 s and at t = 300 s, 25 μL of 10% Triton X-100 was added to lyze all vesicles for the complete destruction of the pH gradient. For data analysis and comparison, time (X-axis) was normalized using Eq. S1. Fluorescence intensities (F_t) were normalized to fractional emission intensity I_F using Eq. S2.

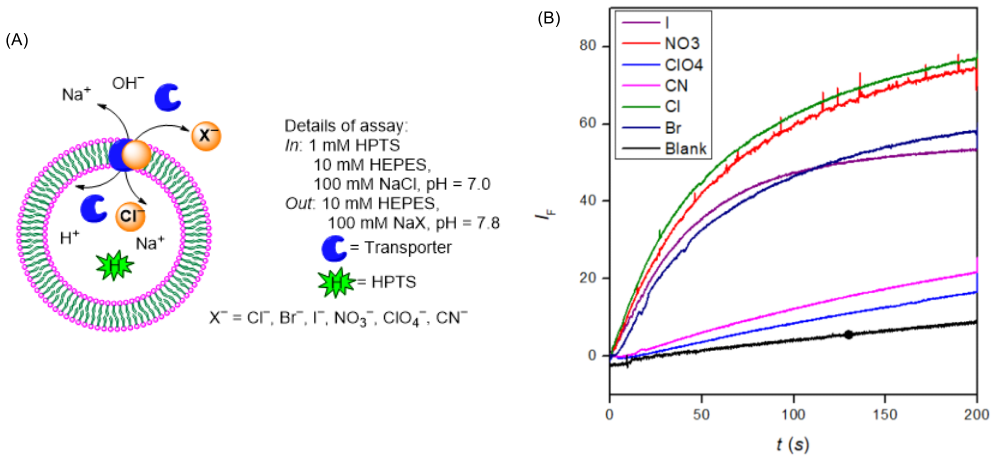

Fig. S5 Schematic representations of fluorescence-based anion assay by changing extravesicular anions (A). Transport activity of **1d** (5.0 μM) by varying extravesicular anions.

Cation selectivity assay: Similarly, cation selectivity of transporter **1d** was explored by changing extravesicular HEPES buffer solution (10 mM HEPES, 100 mM MCl, pH = 7.0) of chloride salts (MCl) of different cations (M = Li^+, Na^+, K^+, Rb^+, and Cs^+). The time axis was normalized according to Eq. S1. The fluorescence data were normalized to percent change in intensity as a course of time using Eq. S2.

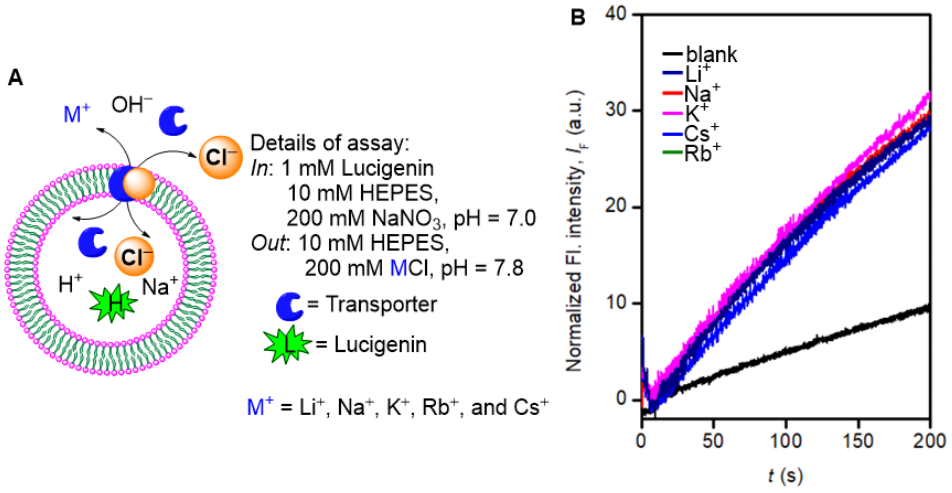

Fig. S6 Schematic representations of fluorescence-based cation selectivity assay (A). Cation selectivity of **1d** (0.3 μM) measured by varying external cations (M^+ = Li^+, Na^+, K^+, Rb^+, Cs^+) across EYPC-LUVs⊃HPTS (B).

Chloride transport activity across EYPC-LUVs⊃lucigenin vesicles

Preparation of EYPC-LUVs⊃lucigenin vesicles: In 10 mL clean and dry round bottom flask, a thin transparent film of egg yolk phosphatidylcholine (EYPC) was formed by drying 1.0 mL

egg yolk phosphatidylcholine (EYPC, 25 mg/mL in $CHCl_3$) with providing continuous rotation and purging nitrogen. The transparent thin film was kept under the high vacuum for 4 h to remove all traces of $CHCl_3$. Then the transparent thin film was hydrated with 1.0 mL aqueous $NaNO_3$ (200 mM, 1.0 mM lucigenin) with occasional vortexing at 10 min intervals for 1 h. The resulting suspension was subjected to freeze and thaw cycles (≥ 15, liquid nitrogen, 55 °C water bath) and 21 times extrusion through 200 nm pore size polycarbonate membrane. The size exclusion chromatography (using Sephadex G-50) was performed to remove extravesicular dye using 200 mM $NaNO_3$ solution as eluent. The collected vesicles suspension was diluted to 4 mL. Inside: 200 mM $NaNO_3$, 1 mM lucigenin, pH = 7.0; outside: 200 mM $NaNO_3$, pH = 7.0.

Ion transport activity by lucigenin assay

In a clean and dry fluorescence cuvette, 200 mM $NaNO_3$ (1975 µL) and EYPC-LUVs⊃lucigenin (25 µL) were taken. This suspension was placed in a slowly stirring condition in a fluorescence instrument equipped with a magnetic stirrer (at t = 0 s). The fluorescence intensity of lucigenin was monitored at λ_{em} = 535 nm (λ_{ex} = 455 nm) as a course of time. The chloride gradient was created by the addition of 2.0 M NaCl (33.3 µL) at t = 20 s between intra- and extravesicular system, followed by the addition of the transporter at t = 100 s. Finally, vesicles were lysed by the addition of 10% Triton X-100 (25 µL) at t = 300 s for the complete destruction of the chloride gradient.

The time axis was normalized according to Eq. S1 and the time-dependent data were normalized to percent change in fluorescence intensity using Eq. S4:

$$I_F = [(I_t - I_0) / (I_\infty - I_0)] \times (-100) \qquad \text{Eq. S4}$$

where, I_0 is the initial intensity, I_t is the intensity at time t, and I_∞ is the final intensity after the addition of Triton X-100.

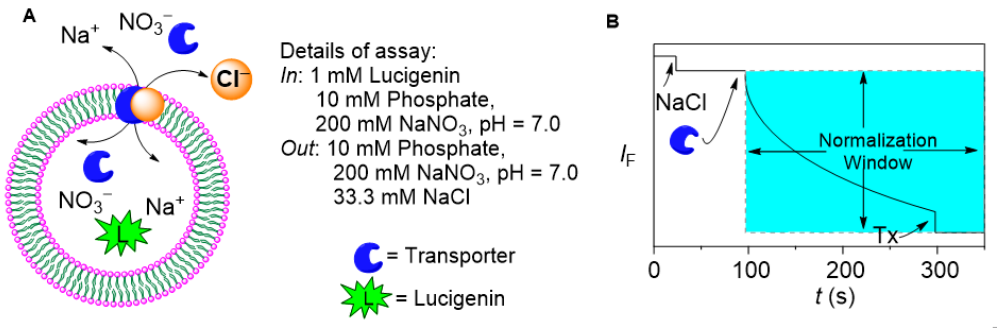

Fig. S7 Representations of fluorescence-based ion transport activity assay using EYPC-LUVs⊃lucigenin (A), and illustration of ion transport kinetics showing normalization window (B).

Ion transport activity across EYPC-LUVs⊃lucigenin in the presence of valinomycin

The antiport mechanism (i.e., simultaneous transport of two different ions, in opposite directions, across the membrane) of **1d** was experimentally confirmed by lucigenin assay in the presence of valinomycin.[S7] The ion transport activity of **1d** was monitored in vesicle entrapped with lucigenin (1 mM) and $NaNO_3$ (200 nM) suspended in KCl (2 M) solution with and without valinomycin. The remarkable enhancement in ion transport activity of **1d** in the presence of valinomycin gave a direct experimental insight into the antiport mechanism of ion transport.

Preparation of EYPC-LUVs⊃lucigenin: The vesicles were prepared by the following protocol as stated above.

Antiport mechanism: In clean and dry fluorescence cuvette, 1975 µL 200 mM $NaNO_3$ solution and 25 µL EYPC-LUVs⊃lucigenin vesicles were taken, and slowly stirred in a fluorescence instrument equipped with a magnetic stirrer (at t = 0 s). The time-dependent fluorescence intensity of lucigenin was monitored at λ_{em} = 535 nm (λ_{ex} = 455 nm). A solution of 2 M KCl (33.3 µL) was added at t = 20 s to create a chloride gradient between intra and extra vesicular system, followed by the addition of valinomycin (1.25 µM) at t = 50 s and transporter **1d** (5 µM) at t = 100 s. Finally, destruction of chloride gradient was done by the addition of 10 % Triton X-100 (25 µL) at t = 300 s. The time axis was normalized according to Eq. S1, and the time-dependent data were normalized to percent change in fluorescence intensity using Eq. S4.

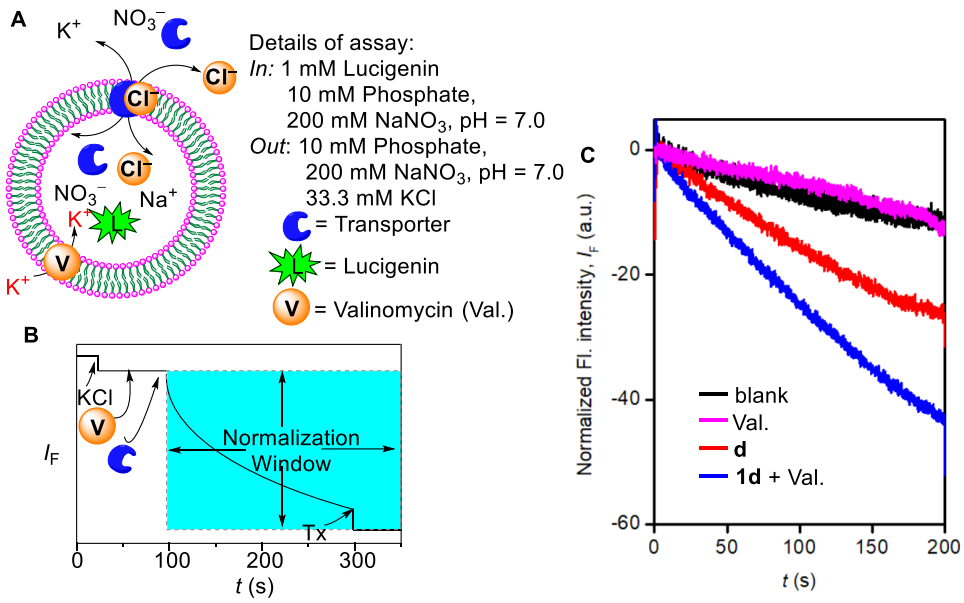

Fig. S8 Schematic representations of fluorescence-based cation selectivity assay (A), and illustration of ion transport kinetics showing normalization window (B). Comparison of Cl^- influx activity of **1d** (5.0 μM) in the absence and in the presence of valinomycin (1.25 μM) (C).

Proof of antiport mechanism by lucigenin assay in the presence of external SO_4^{2-} and NO_3^- anions

Preparation of EYPC-LUVs⊃lucigenin vesicles: In a 10 mL clean and dry round bottom flask, the thin transparent film of egg yolk phosphatidylcholine (EYPC) was formed by drying 1.0 mL egg yolk phosphatidylcholine (EYPC, 25 mg/mL in $CHCl_3$) with providing continuous rotation and purging nitrogen. The transparent thin film was kept under a high vacuum for 4 h to remove all traces of $CHCl_3$. Then the transparent thin film was hydrated with 1.0 mL aqueous NaCl (200 mM, 1.0 mM Lucigenin) with occasional vortexing at 10 min intervals for 1 h. The resulting suspension was subjected to freeze and thaw cycles (≥ 15, liquid nitrogen, 55 °C water bath) and 21 times extrusion through 200 nm pore size polycarbonate membrane. The size exclusion chromatography (using Sephadex G-50) was performed to remove extravesicular dye using 200 mM NaCl solution as eluent. The collected vesicles suspension was diluted to 4 mL. Final conditions: ~ 5 mM EYPC; inside: 200 mM NaCl, 1 mM lucigenin, pH 7.0; outside: either 200 mM $NaNO_3$ or 200 mM Na_2SO_4.

Ion transport assay

In a clean and dry fluorescence cuvette, either 200 mM of $NaNO_3$ or 200 mM of Na_2SO_4 (1975 μL) and EYPC-LUVs⊃lucigenin (25 μL) were taken. This suspension was placed in a slowly

stirring condition in a fluorescence instrument equipped with a magnetic stirrer (at $t = 0$ s). The fluorescence intensity of lucigenin was monitored at λ_{em} = 535 nm (λ_{ex} = 455 nm) as a course of time. The transporter molecule **1d** was added at t = 100 s. Finally, vesicles were lysed by adding 10% Triton X-100 (25 μL) at $t = 300$ s for the complete destruction of chloride gradient. NO_3^- transport occurred with the concomitant efflux of Cl^- ions, and on the other hand, SO_4^{2-} being more hydrophilic is not transported easily, suggesting the operation of antiport mechanism.

The time axis was normalized using Eq. S1, and the time-dependent data were normalized to percent change in fluorescence intensity using Eq. S2.

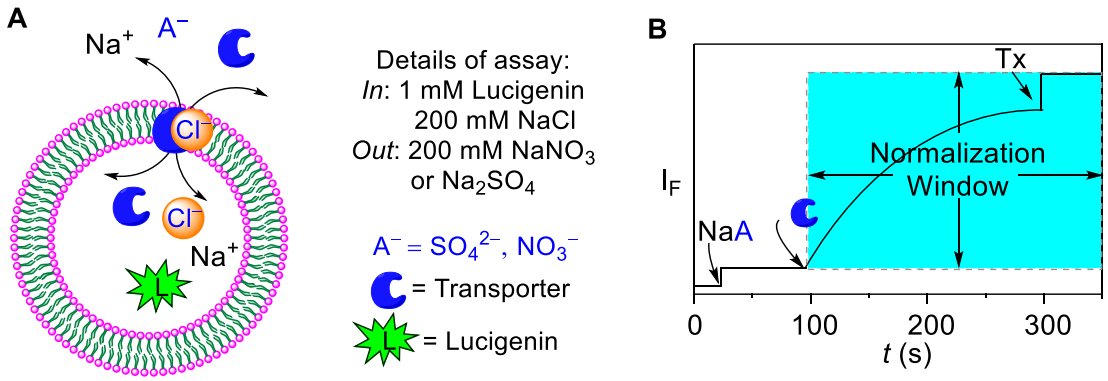

Fig. S9 Representation of fluorescence-based antiport assay using EYPC-LUVs⊃lucigenin (A). Representation of ion transport kinetics showing normalization window (B).

V. Photoisomerization Studies by UV-Vis and ^{1}H NMR

A. UV-Vis studies

Photoisomerizations of compounds **1a**, **1b**, **1c** and **1d** were carried out in CH_3CN. Initially, stock solutions of these compounds (2 mM in DMSO) were prepared in different vials, and covered with an aluminium foil.

In a 2 mL UV cuvette, was placed either 1900 μL of CH_3CN and 20 μL of either **1a**, **1b**, **1c** or **1d** (2 mM in DMSO) was added to get the final concentration of 100 μM.

The cuvette was placed in a UV-Vis spectrometer and the UV-Vis spectrum was recorded.

***trans* to *cis* Isomerization:** Subsequently, each of these samples was irradiated at λ = 365 nm using LEDs (3 × 1/3 Watt) for varied time intervals to isomerize the azobenzene moiety. After each irradiation, the UV-Vis spectrum was recorded. Subsiquently, the photoisomerized

samples were photoirradiated at λ = 365 nm using LEDs (3 × 1/3 Watt) and again after each irradiation, the UV-Vis spectrum was recorded.

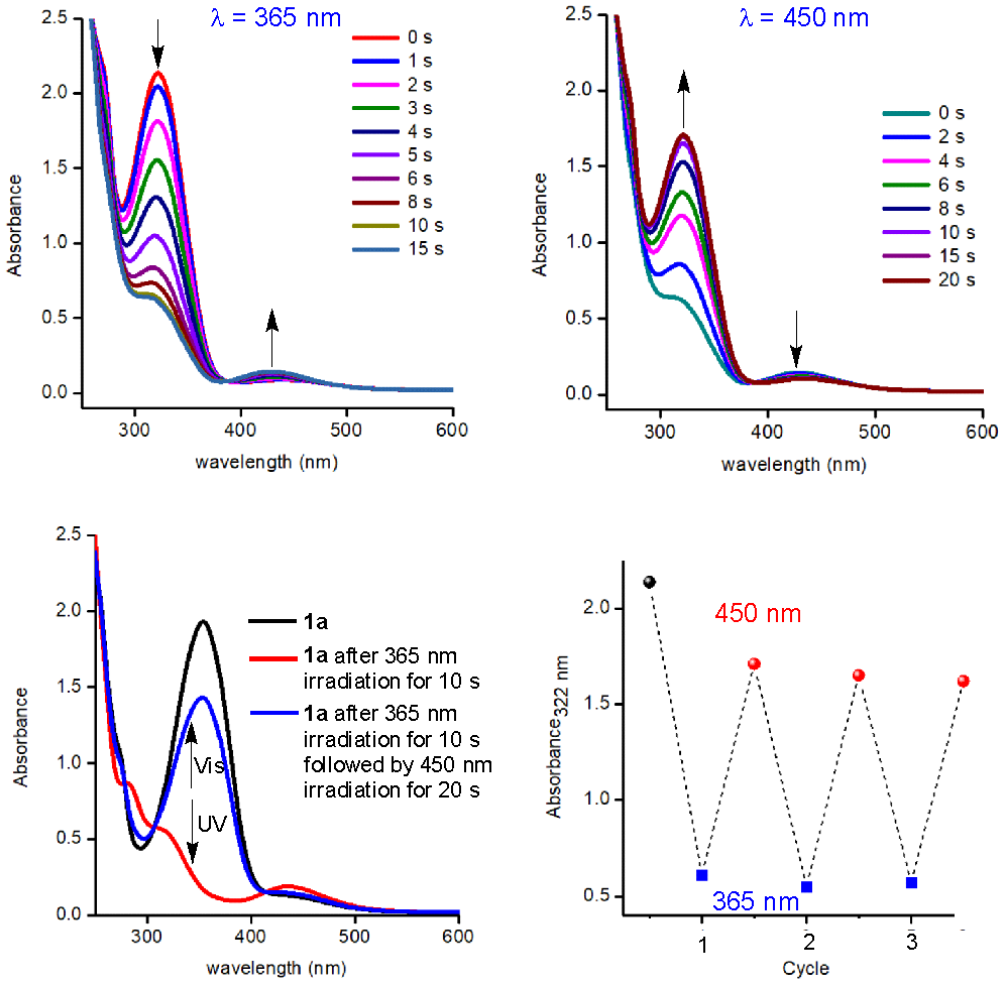

Fig. S10 UV-visible spectral changes for **1a** (20 μM) upon irradiation with 365 nm light (3 × 3 Watt LEDs) (A). UV-visible spectral changes for **1a** (20 μM) upon irradiation with 450 nm light (3 × 3 Watt) (B). Comparison of UV-visible spectra of **1a** (20 μM) upon irradiation with 365 nm light for 10 s, and **1a** (20 μM) upon irradiation first with 365 nm light for 10 s followed by irradiation with 450 nm light for 20 s (C). Switching cycles for **1a** (20 μM) under alternating irradiation with 365 nm and 450 nm lights (D). The absorbance at 380 nm was monitored for the switching study. All data were recorded in CH_3CN.

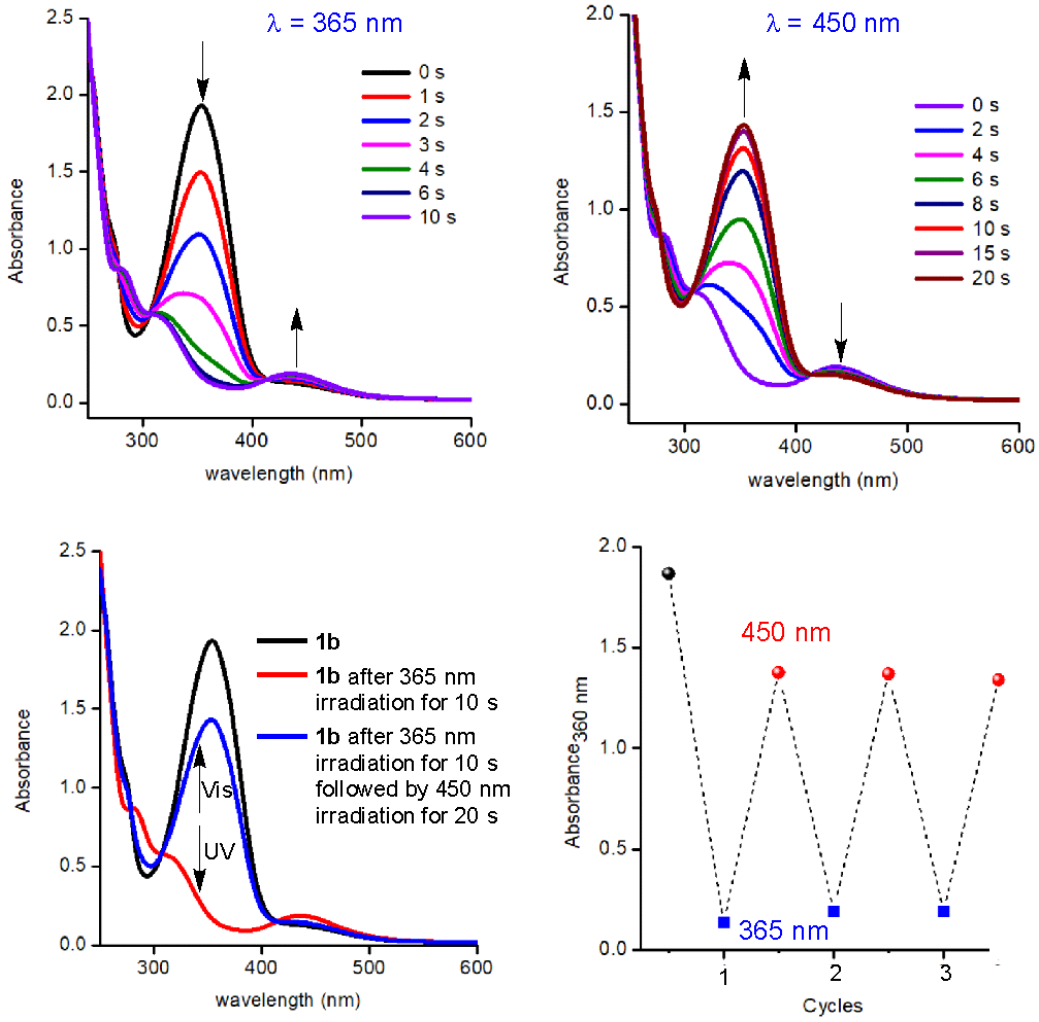

Fig. S11 UV-visible spectral changes for **1b** (20 μM) upon irradiation with 365 nm light (3 × 3 Watt LEDs) (A). UV-visible spectral changes for **1b** (20 μM) upon irradiation with 450 nm light (3 × 3 Watt) (B). Comparison of UV-visible spectra of **1b** (20 μM) upon irradiation with 365 nm light for 10 s, and **1b** (20 μM) upon irradiation first with 365 nm light for 10 s followed by irradiation with 450 nm light for 20 s (C). Switching cycles for **1b** (20 μM) under alternating irradiation with 365 nm and 450 nm lights (D). The absorbance at 380 nm was monitored for the switching study. All data were recorded in CH_3CN.

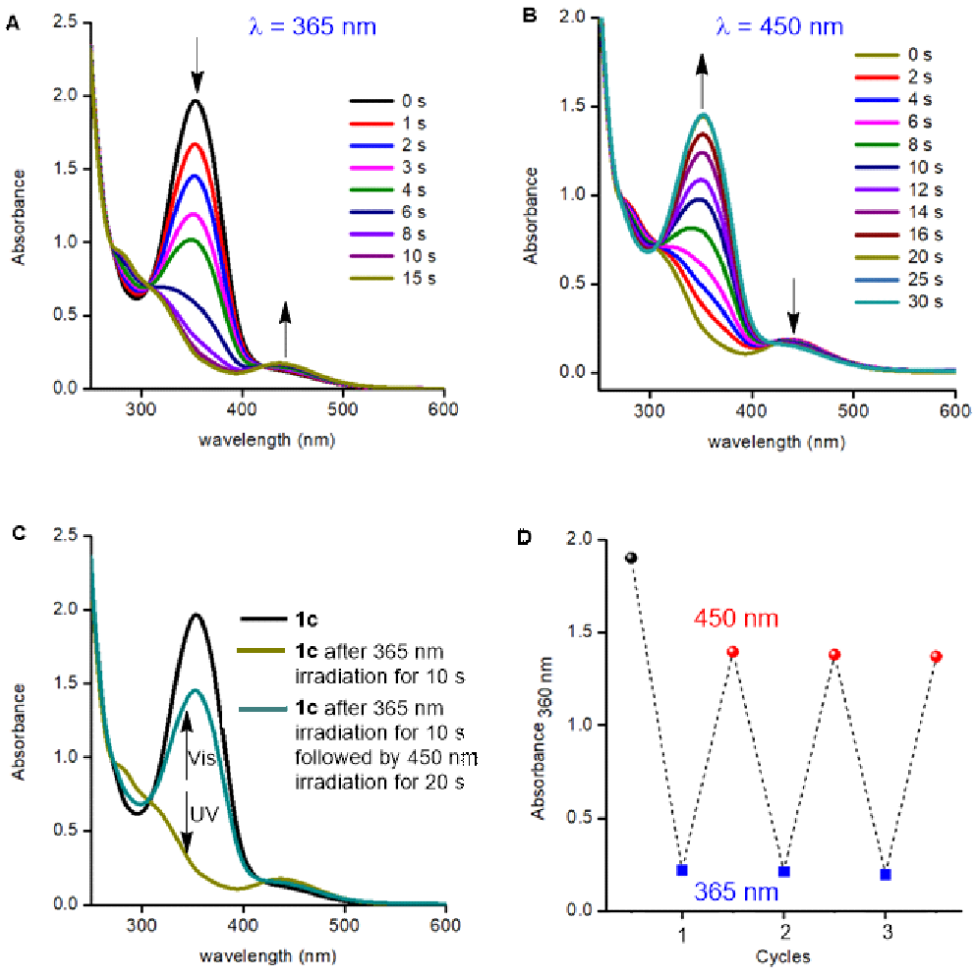

Fig. S12 UV-visible spectral changes for **1c** (20 μM) upon irradiation with 365 nm light (3 × 3 Watt LEDs) (A). UV-visible spectral changes for **1c** (20 μM) upon irradiation with 450 nm light (3 × 3 Watt) (B). Comparison of UV-visible spectra of **1c** (20 μM) upon irradiation with 365 nm light for 10 s, and **1c** (20 μM) upon irradiation first with 365 nm light for 10 s followed by irradiation with 450 nm light for 20 s (C). Switching cycles for **1c** (20 μM) under alternating irradiation with 365 nm and 450 nm lights (D). The absorbance at 380 nm was monitored for the switching study. All data were recorded in CH_3CN.

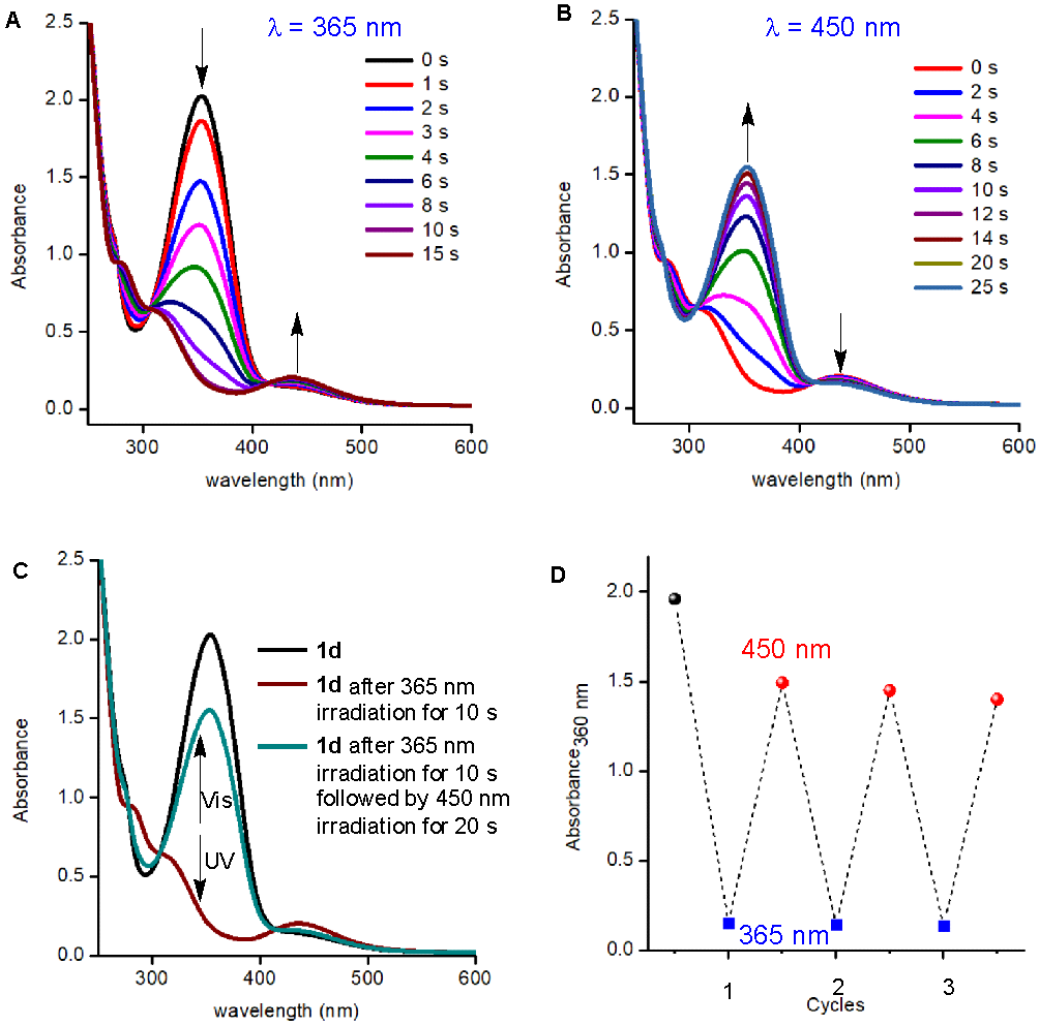

Fig. S13 UV-visible spectral changes for **1d** (20 μM) upon irradiation with 365 nm light (3 × 3 Watt LEDs) (A). UV-visible spectral changes for **1d** (20 μM) upon irradiation with 450 nm light (3 × 3 Watt) (B). Comparison of UV-visible spectra of **1d** (20 μM) upon irradiation with 365 nm light for 10 s, and **1d** (20 μM) upon irradiation first with 365 nm light for 10 s followed by irradiation with 450 nm light for 20 s (C). Switching cycles for **1d** (20 μM) under alternating irradiation with 365 nm and 450 nm lights (D). The absorbance at 380 nm was monitored for the switching study. All data were recorded in CH_3CN.

^{1}H NMR studies

***Trans* (*E*) to *cis* (*Z*) photoisomerization:** For monitoring the *trans* (*E*) to *cis* (*Z*) isomerization by ^{1}H NMR, a sample of **1a**, **1b**, **1c**, or **1d** (4.0×10^{-3} M) in CD_3CN was prepared in an NMR tube and then irradiated at λ = 312 nm using UV tubes (8 × 3 Watt) for 30 min and then the ^{1}H NMR data before and after photoirradiation were compared. The *trans* to *cis* ratio after photoirradiation for **1a**, **1b**, **1c**, and **1d** were 08:92, 10:90, 12:88, and 11:89, respectively.

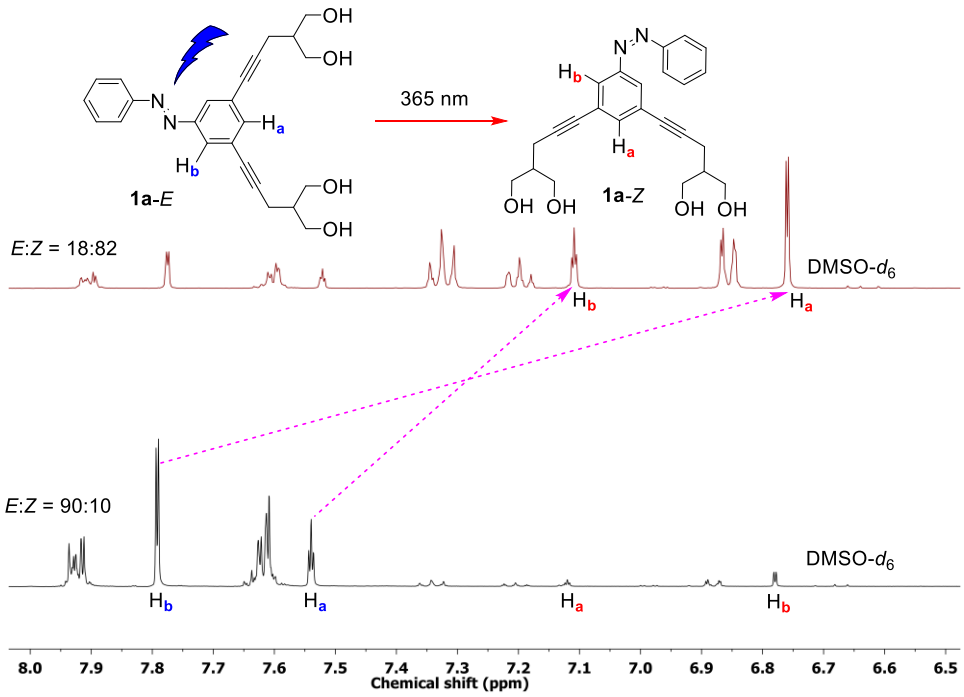

Figure S14. Partial ^{1}H NMR spectrum of **1a** (*E*:*Z* of 90:10, concentration = 4.0 × 10^{-3} M, down) in DMSO-d_6 at 25 °C, and that of photo-irradiated sample of **1a** (up) by 365 nm light for 10 min. The *trans* to *cis* ratio after photo-irradiation is 18:82.

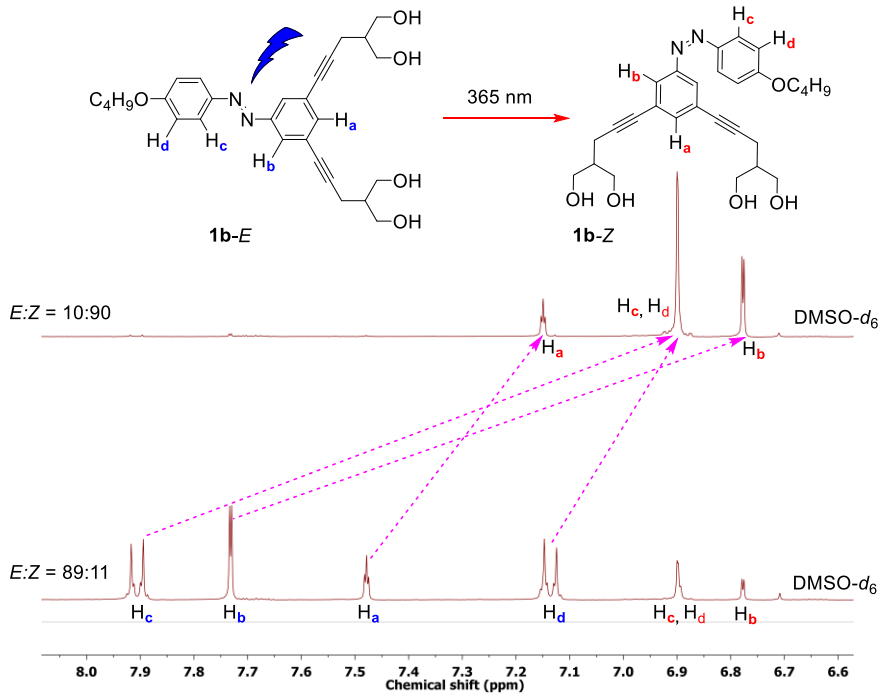

Figure S15. Partial ^{1}H NMR spectrum of **1b** (*E*:*Z* of 89:11, concentration = 4.0 × 10^{-3} M, down) in DMSO-d_6 at 25 °C, and that of photo-irradiated sample of **1b** (up) by 365 nm light for 10 min. The *trans* to *cis* ratio after photo-irradiation is 10:90.

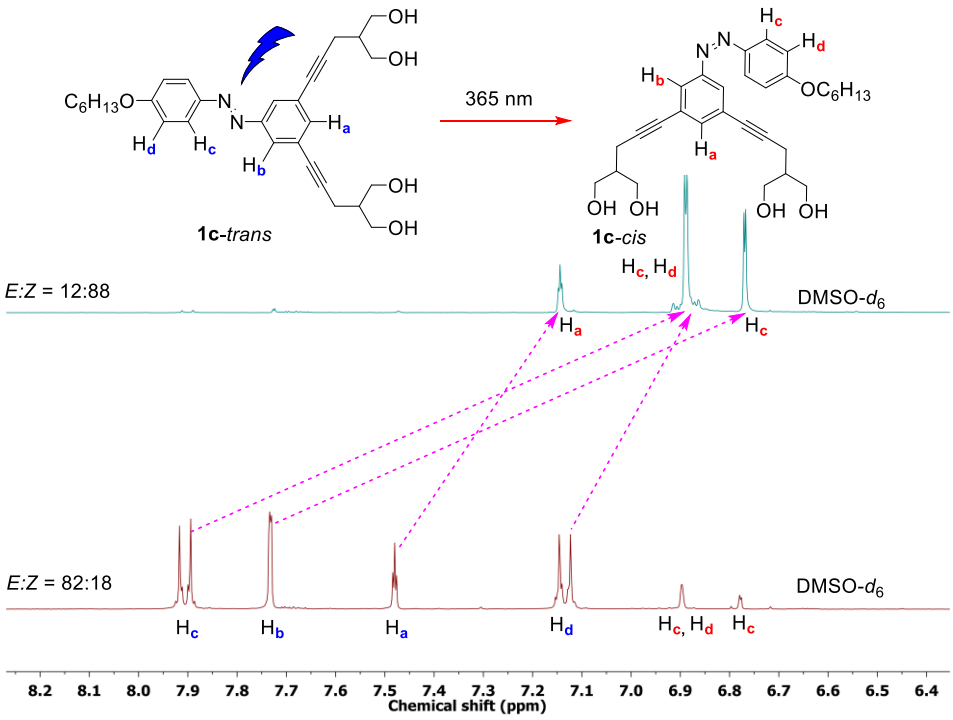

Figure S16. Partial ^{1}H NMR spectrum of **1c** (*E*:*Z* of 82:18, concentration = 4.0 × 10^{-3} M, down) in DMSO-d_6 at 25 °C, and that of photo-irradiated sample of **1c** (up) by 365 nm light for 10 min. The *trans* to *cis* ratio after photo-irradiation is 12:88.

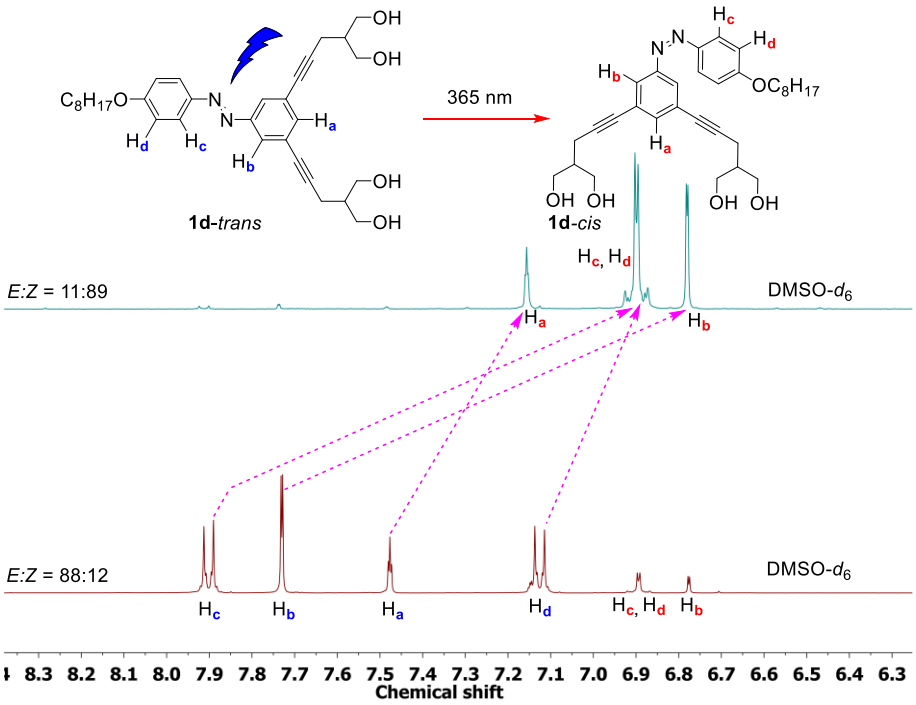

Figure S17. Partial ^{1}H NMR spectrum of **1d** (*E*:*Z* of 88:12, concentration = 4.0 × 10^{-3} M, down) in DMSO-d_6 at 25 °C, and that of photo-irradiated sample of **1d** (up) by 365 nm light for 10 min. The *trans* to *cis* ratio after photo-irradiation is 11:89.

Thermal stability

In order to check the thermal stability of photoisomerized *cis* form, In a 3 mL UV cuvette was placed 1980 µL of acetonitrile and 20 µL of **1d** (2 mM in DMSO) was added to get the final concentration of 20 µM. Initially, the UV-Vis absorbance was recorded for the *trans* form. Subsequently, the sample was irradiated at λ = 365 nm using LEDs (3 × 3 Watt) for 10 s to achieve *trans* to *cis* photoisomerization and absorbance was again recorded. The photoisomerized *cis* sample was then kept in dark and UV-Vis absorbance was recorded after each 1 h. The process was repeated for a total of 9 h.

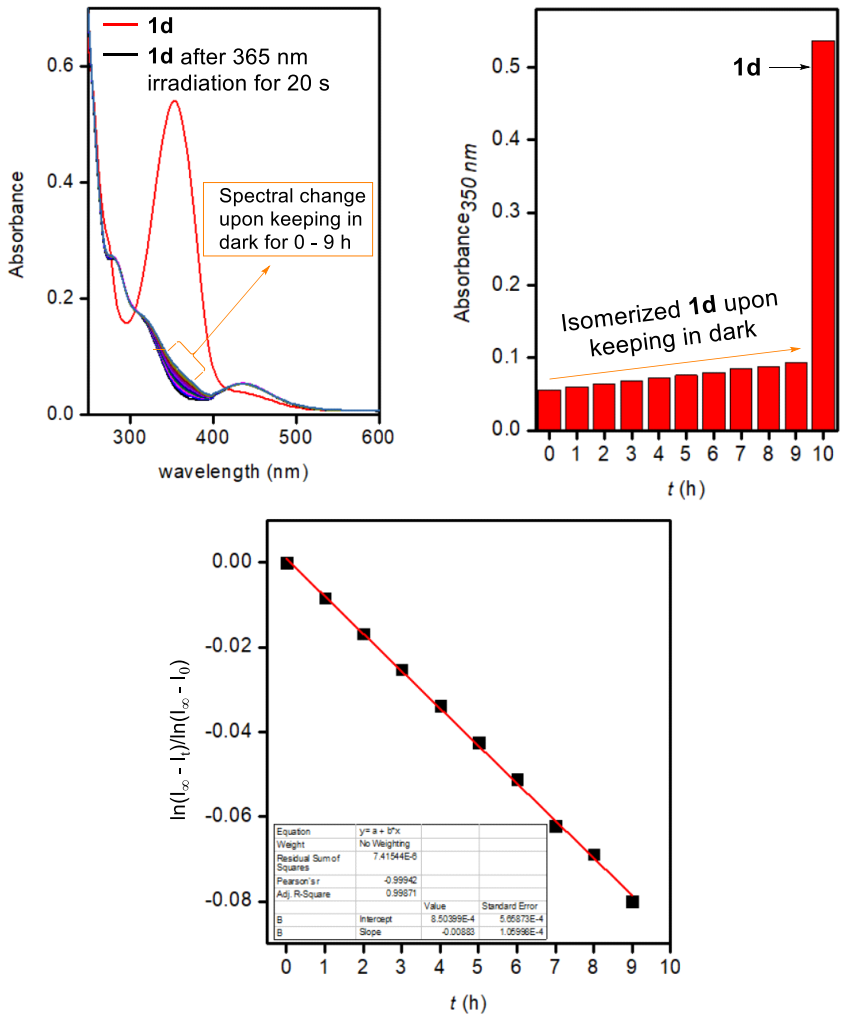

Fig. S18 UV-visible spectral change for **1d** (20 µM) upon irradiation with 365 nm light (3 × 3 Watt LEDs) and upon keeping in dark for 9 h (A). Change in absorption at (A_{350}) of **1d** (20 µM) upon keeping in dark for 9 h (B). Plot of $\ln(I_\infty - I_t)/ \ln(I_\infty - I_0)$ as a function of time to determine the half-life for thermal *cis* to *trans* isomerisation for **1d**. The half-life comes out to be 113 ± 5 h, which has been calculated from three independent experiments (C).

VI. Photoregulatory Ion Transport Activity

The EYPC-LUVs⊃HPTS vesicles were prepared using the same protocol as stated above. In a clean and dry fluorescence cuvette, 100 mM NaCl (1975 μL) and EYPC-LUVs⊃HPTS (25 μL) were taken. This suspension was placed in a slowly stirring condition in a fluorescence instrument equipped with a magnetic stirrer. The fluorescence intensity of HPTS was monitored at λ_{em} = 510 nm (λ_{ex} = 450 nm) as a course of time. The pH gradient was created by the addition of 2.0 M NaOH (25 μL) at t = 20 s between intra- and extravesicular system, followed by the addition of transporters (**1d**) at t = 100 s. Finally, vesicles were lysed by addition of 10% Triton X-100 (25 μL) at t = 300 s for the complete destruction of the pH gradient. Initially, the transport activity of either of the compound **1d** (0.25 μM, using stock solution of 2 mM in DMSO was recorded. Subsiquently, the stock samples were irradiated at λ = 365 nm using LEDs (3 × 1/3 Watt) for different time intervals to photoisomerize the azobenzene subunit and the transport activity was recorded after each irradiation process. Photoisomerization leads to a substantial decrease in the transport activity. After that, the photoisomerized sample were irradiated at λ = 450 nm using LEDs (3 × 1 Watt) for different time intervals and the transport activity was recorded after each irradiation process. The photoirradiation at 450 nm lead to the substantial regeneration of the initial ion transport activity. This photo-regulatory transport activity behavior of the transporter **1d** was repeated for several cycles without the loss of efficiency.

The time-dependent data were normalized to percent change in fluorescence intensity using Eq. S4:

$$I_F = [(I_t - I_0) / (I_\infty - I_0)] \times (100) \qquad \text{Eq. S2}$$

where, I_0 is the initial intensity, I_t is the intensity at time t, and I_∞ is the final intensity after addition of Triton X-100.

We also performed the anion selectivity of **1d** upon photoisomerization and same trend of ion selectivity was observed (Figure S19E). It shows that ion transport activity in the *cis* form is most likely due to non-photoisomerized trans form at *E*/*Z* photostationary state rather than arising from the *cis* isomer.

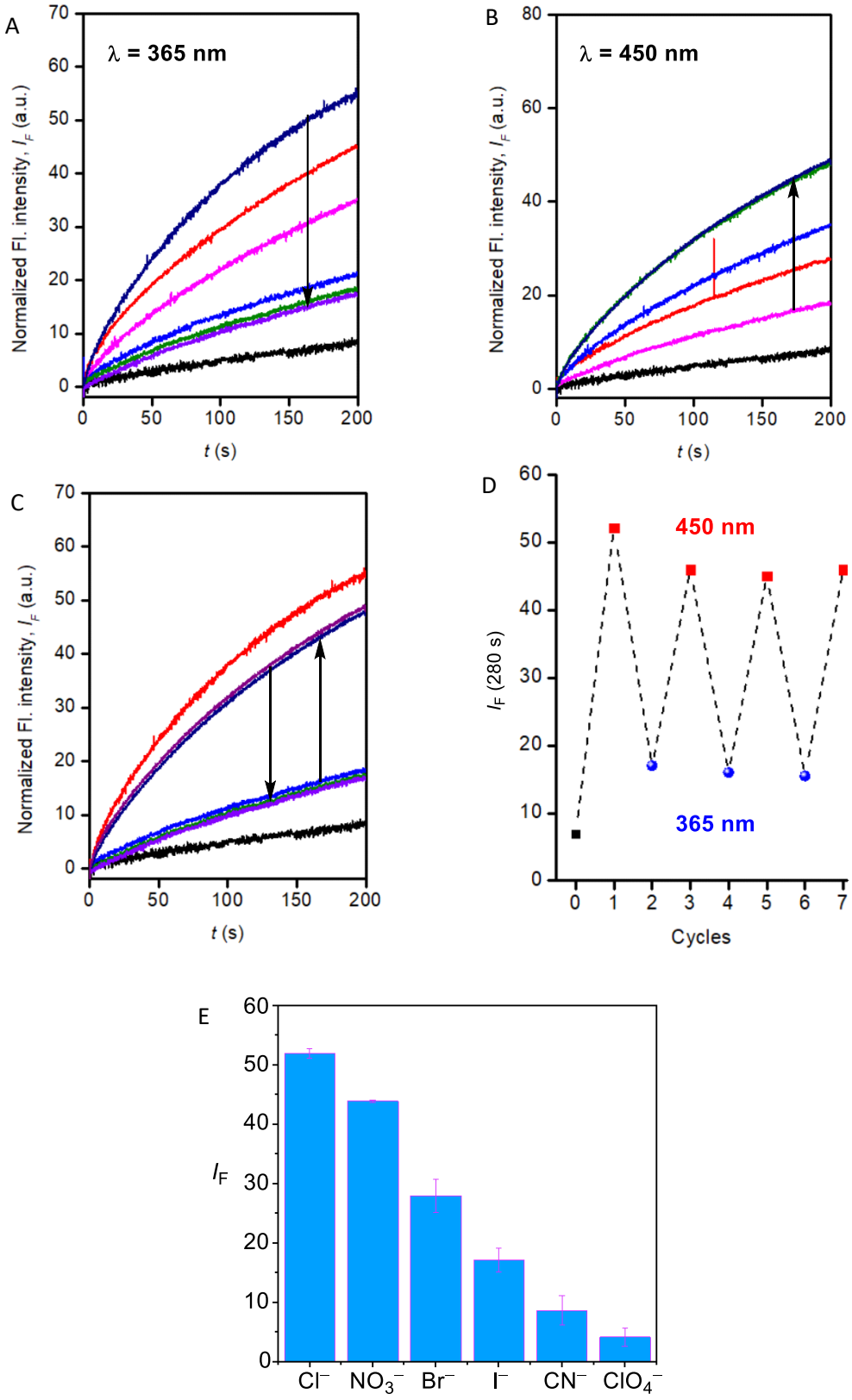

Figure S19. Change in the transport activity of **1d**-*E* (0.25 μM) upon photoirradiation at 365 nm using LEDs (3 × 1/3 Watt) for 0 to 15 sec across EYPC-LUVs⊃HPTS (A). Change in the transport activity of **1d**-*Z* (0.25 μM) upon photoirradiation at 450 nm using LEDs (3 × 1/3

Watt) for 0 to 20 sec across EYPC-LUVs⊃HPTS (B). Photo regulated transport activity of **1d** (0.25 μM) upon alternating photo irradiation at two different wavelengths of 365 nm and 450 nm, respectively (C). Photo regulated transport activity of **1d** (0.25 μM) at *t* = 280 s (D). Anion selectivity of **1d** in *cis* form at (3.0 mM) (E).

VII. FESEM Studies

The surface morphology of the compound in solid state was examined by FESEM studies. For *trans* form, the compound **1d** was dissolved in methanol solvent system to prepare a 150 μM solution. The compound solution was drop-casted on silicon wafer, dried and then used for FESEM studies. On the other hand, for *cis* form, compound 1d in methanol was photo irradiated for 20 min using 365 nm LEDs and then drop-casted on silicon wafer, dried and then used for FESEM studies.

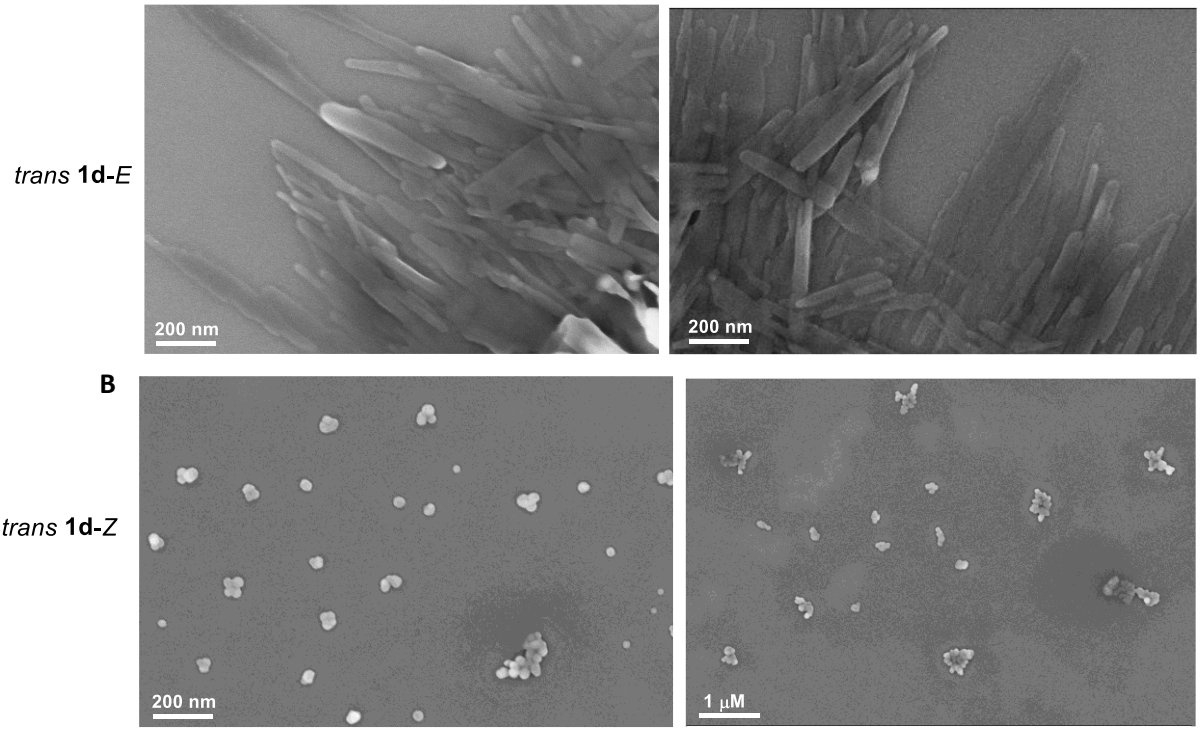

Fig. S20 FESEM images of **1d**-*E* (A) and **1d**-*Z* (B) showing distinct aggregation patterns recorded in methanol.

VIII. Planar Bilayer Conductance Measurements

The conductance measurement across the bilayer lipid membrane was done with the help of Warner instrument (USA). For that, a solution of diphytanoylphosphatidylcholine lipid

(DPhPC; Avanti Polar Lipids) was prepared by dissolving it in *n*-decane of concentration 20 mg/mL. Then a bilayer membrane was formed by using this solution at the 150 μm diameter aperture within a cup made of polystyrene (Warner Instrument, USA). In both chambers (*cis* and *trans*) of the instrument, 1 M KCl was symmetrically injected. The set up was made in such a way that the *trans* compartment was held at virtual ground. The BC *535* head−stage (Warner Instrument, USA) connects the *cis* compartment through Ag-AgCl electrodes. Then the channel-forming molecule **1d (**20 μM) was added to the *trans* chamber. An inbuilt magnetic stirrer was used to stir the solution for 20 min. Channel formation through the lipid bilayer was confirmed from channel opening and closing events upon application of different voltages using pClamp11 software (Molecular probes, USA). An analogue-to-digital converter (Digidata 1440A, Molecular Devices) and pClamp11 software (Molecular probes, USA) were used to low pass filter the currents at 1 kHz.

The channel opening and closing events at positive, as well as negative potentials, were analysed by pClamp software (v. 10.6). A complete trace comprised of a series of opening and closing events for the time period of 2 h from where a small fraction is presented in the manuscript.

The channel diameter was calculated using the Eq. (Hille Eq.) mentioned below.[S8]

$$1/g = (l + \pi d/4)\,(4\rho/\pi d^2) \qquad \text{Eq. S6}$$

Where, g is the corrected conductance, calculated by multiplying measured single-channel conductance with the Sansom's correction factor[S9] 5.61; l is the length of the ion channel (34 Å), and ρ signifies resistivity of the KCl solution (ρ = 10.1 Ω·cm).

Determination of anion selectivity permeability ratio by Planar Bilayer Conductance Measurements: The *cis* and *trans* chambers were filled with unsymmetric solutions of KCl. The *cis* chamber was filled with 1.0 M KCl solution and the *trans* chamber was filled with 0.5 M KCl. The compounds **1d (**2 μM) were added to the *trans* chamber and stirred for 5 min. The permeability ratio (P_{Cl^-}/P_{K^+}) was calculated by using the Goldman-Hodgkin-Katz Eq. (Eq. S7).[8]

$$\frac{P_{Cl^-}}{P_{K^+}} = \frac{a_{K^+}{}_{cis} - a_{K^+}{}_{trans} \times \exp\left(-\frac{Z \times V_{rev} \times F}{R \times T}\right)}{a_{Cl^-}{}_{cis} \times \exp\left(-\frac{Z \times V_{rev} \times F}{R \times T}\right) - a_{Cl^-}{}_{trans}} \qquad \text{Eq. S7}$$

where, P_{Cl-}/P_{K+} = anion/cation permeability ratio; $a_{K^+\,cis}$ = K^+ activity in the *cis* chamber; $a_{K^+\,trans}$ = K^+ activity in the *trans* chamber; $a_{Cl^-\,cis}$ = Cl^- activity in the *cis* chamber; $a_{Cl^-\,trans}$ = Cl^- activity in the *trans* chamber[S10]; Z_{K^+} = +1, Z_{Cl^-} = –1, V_{rev} = reversal potential; F = Faraday constant; R = gas constant; T = temperature (K).

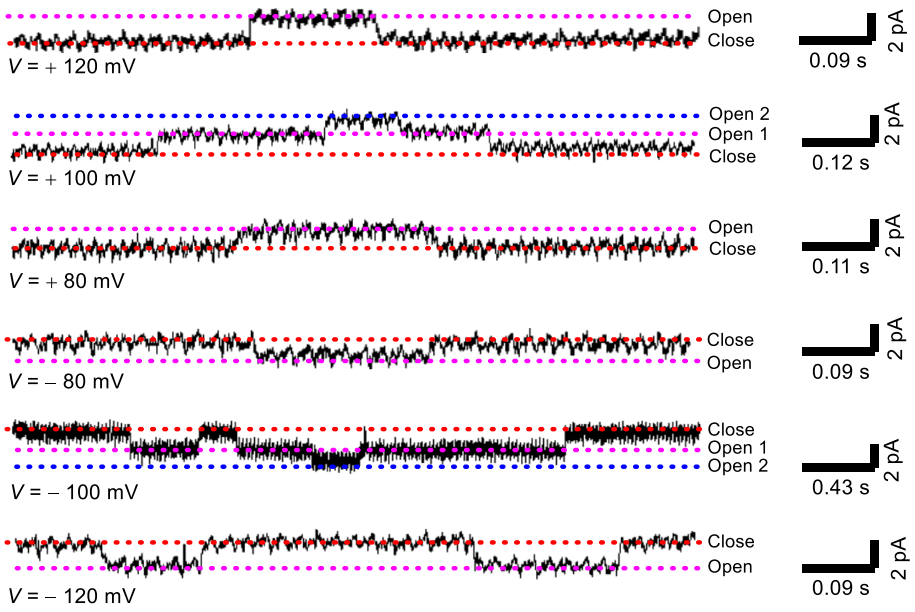

Fig. S21 The single channel current traces by **1d** (20 μM) recorded at various negative and positive potentials under symmetrical KCl solution.

IX. Theoretical Studies

To explore the underlying mechanism of ion passage through the channel and to assess the stability of the channel on or before the ion transport, atomistic computer simulations are performed. To comment on the possibility of transportation of ion though the channel constituted with the monomers in either *cis* or *trans* form, we have compared the relative stabilty of each of the channel (*cis*/*trans*) during our simulation.

Model and Methods

System setup and simulation model: Initially, the coordinates of both the *cis* and *trans* channel structures (composed of six consecutive layers) were minimised by utilization of MAESTRO. [S11] These semi-minimised structures were further used in constitution of the corresponding channel/membrane complex with the help of the membrane builder protocol in CHARMM-GUI.[S12] The protocol involves multiple steps described by Jo et al[S13] first reading the object followed by its suitable orientation and then constitution of lipid bilayer assembly

(first constitution and then assembly) after determination of system size, and finally system equilibration. The generated channel/membrane complex comprises of the membrane-embedded self-assembled channel structure (situated at the centre of lipid membrane) which is made up of 12 monomers arranged in six repetitive layers. The bilayer membrane contains 1, 2-diphytanoyl-*sn*-glycero-3-phosphocholine (DPhPC) lipids in 144 units total which is distributed in equal number over each of the leaflet (the membrane leaflets contains 72 number each). Towards the end, the channel/membrane constitution was incorporated in a rectangular box with dimension $7.7 \times 7.7 \times 9.0$ nm^3. Finally both the compartments of the system separated by the lipid bilayer, was solvated with water and 1 M KCl was added to each of the aqueous compartments. The details of both the simulation systems containing *cis* and *trans* channel structures individually are shown in Table 1.

Table 1. Simulation studies of **1d** in *trans* and *cis* forms.

System	Box dimension	No. of water molecules	No. of K^+ ions	No. of Cl^- ions
Cis channel	7.8x7.8x9.0 nm^3	9985	175	175
Trans channel	7.8x7.8x9.0 nm^3	9749	175	175

The general AMBER forcefield (GAFF) were employed to model each of the channel (*cis*/*trans*). [S14] For modelling the membrane the CHARMM36m forcefield parameters; [S15, S16] are used. The CHARMM-TIP3P[S17] water model was emplyed in our simulation.

Simulation method: The periodic boundary conditions (PBC) was applied for each of the simulations in all three dimensions (along x, y and z directions). Long-range electrostatic interactions were employed using the particle mesh Ewald (PME) method[S18] (with cubic interpolation). Short-range electrostatic interactions were set with the cut-off of 1.2 nm. During the simulation the neighbour lists were updated at a frequency of 20 steps. Each bonds with hydrogen atoms (of membrane and channel monomers) were constrained with the LINCS algorithm[S19] Water molecule rigidity was maintained using the SETTLE[S20] algorithm. For Lenard Jones interactions the Verlet cut-off scheme[S21] was employed with a cut-off of 1.2 nm considering dispersion corrections involved. Initially the system was energy minimized with particular restraints via the steepest-decent algorithm followed by six successive steps equilibration of duration 10 ns each. During the equilibration process the restraint over the system was gradually reduced in each of the consecutive step. An average temperature of 298

K and pressure of 1.0 bar were maintained during the equilibration process by using Berendsen thermostat[S22] and Berendsen barostat. After equilibration, each of the system was taken for the final NPT production run for 1.0 microsecond under slight restrain condition (applied on each of the channel structures). During production simulation, the 298 K average temperature was fixed using Nose-Hoover thermosta[S23] via a relaxation constant of 1.0 ps. The channel, membrane bilayer, and solvent were by individually coupled to thermostat. The pressure was maintained at 1.0 bar with the help of Parrinello-Rahman barostat[S24] (with 5 ps coupling constant and the compressibility factor of 4.5 × 10-5 bar) under semi-isotropic coupling (coupled separately XY and Z directions) condition to confirm tensionless bilayer during the course of simulation. The time step of 2 fs (production run) was chosen utilizing leapfrog integrator. Each of the channel (*cis* and *trans*) structures are simulated following similar protocol. Simulations of both the systems are replicated twice. All the simulations are performed using GROMACS software of 20x version.

Free energy simulation: To compute the free energy of chloride ion transport through the channel (*trans*) umbrella sampling simulation was performed. For understanding the underlying mechanism of ion transport process, only one chloride ion was taken for transportation along the channel core and a set of configurations were generated (to initiate umbrella sampling) corresponding to the different position of the anion spanning along the channel lumen (starting from the entry of the anion through the channel mouth, followed by final exit of the anion via the other end of the channel).

For maintaining the electro-neutrality of the system, one K^+ ion is inserted into the system. During umbrella sampling simulation, the dimension of the simulation box and number of water molecules were kept same as the previously described equilibrium simulation for each of the channel system (*cis* and *trans*). For umbrella sampling simulation, the collective variable (CV) was considered along the Z-direction of the chloride anion with respect to the channel (excluding hydrogen atoms), d (Fig. 5E, Manuscript). Negative value of d indicates the position of the anion at upper half of the channel i.e. above the center of the channel (when the ion travels towards mouth of the channel from its centre) while positive d points the anion location at the lower half of the channel i.e. below the center of the channel structure (when the anion passage from centre o the end of the channel). The position of the anion at the mid-position (at the centre of the channel structure) is referred as d = 0 nm. Configurations were generated with respect to the CV ranging from -1.5 nm to 3.0 nm at a spacing of 0.1 nm of d. Simulation at each of the umbrella sampling windows are performed at force constant ranging from 7500 to

9000 kJ/mol/nm^2 to maintain the respective position of the anion at the specified value. At first, each of the configurations (traditionally referred as 'windows') were energy minimized with steepest-descent algorithm followed by 500 ps of equilibration (simulation time step of 1 fs) in NVT ensemble. Finally each of the equilibrated systems were considered for final NPT production run (with 2 fs time step) of 20 ns in each of the windows. During the umbrella sampling simulation in each of the windows 298.15 K of average temperature and 1 bar average pressure were maintained employing the same thermostat and barostat employed during equilibration and production run, as was utilized for the case of equilibrium simulation. For calculation of the respective equilibrium free energy profile, the weighted histogram analysis method (WHAM) was applied. GROMACS software of version 20x were employed to execute each of the simulation.

Along with computation of the free energy profile, to explore the underlying the molecular mechanism of the chloride ion transport process the number of contacts were analysed between the channel components and the passing anion. The calculation of root mean square deviation (RMSD) was performed for each of the channel structures to assess the relative stabilities. For investigation the role of the water in the transport process, number of water molecule(s) present around the passing chloride ion was calculated.

First we have estimated the stability of each of the channel structures (*cis* and *trans*) and compared the time profile of root mean square deviation (RMSD) during equilibrium simulation for both the channels (Fig. 5c, Manuscript).

From Fig., it is evident that RMSD of the channel constituted with the *cis* monomers is higher compared to that of the *trans* channel. This suggests that the *trans* channel structure, in constituted state in lipid membrane, remains relatively more stable compared to that of the *cis* superstructure. The snapshots in Fig. 5A, B in Manuscript also refers to the relatively more stability of the channel made up from the *trans* monomers than that of the *cis* form.

Our simulation result suggesting the higher stability of *trans* channel is in agreement with the experimental finding on the same. Further after examining the relative thermodynamic stability of the channels, we proceeded to compute the free energy of the anion transport through the stable *trans* structure. From the free energy profile (Fig. 5F, Manuscript), it is evident that the free energy becomes maximum when the chloride ion remains at the middle of the channel, while the free energy decreases gradually when the anion moves towards the either end of the

channel structure, which is being reflected by the fairly symmetric nature of the free energy profile on either side.

The progress of the anion becomes slower at the channel-center leading to the increased free energy barrier. On the other hand, when the ion approaches the bulk water interface, the free energy barrier is lowered considerably, due to its favourable interaction with the enough number of water molecules. The lesser availability of solvent molecules inside channel core, especially at its central part, gives rise to a relatively unfavourable environment for the chloride ion with respect to the ion at the either end of the channel (near the bulk water). Fig. S22 represents the number of water molecules associated with the chloride ion during the transport process. With the movement of the anion from the bulk water environment through the channel core, the number of water molecules around the anion slowly decreases and as it reached to the center of the channel it is decreased most. It is observed that while the number of water accompanying the passing ion decreases as the ion passes through the channel, it does not drop down to zero. This is the reason why the anion would not be completely at an unfavourable

desolvated condition at the center of the channel and hence the free energy barier for the Cl^- transport through the channel remains managably low i.e., only ~ 11 kcal/mol (Fig. 5f, Manuscript). In other words, the presence of sufficient amount of water within the channel core is actually assisting the ion to get transported through the channel by maintaining a favorable solvent-rich environment, thereby not letting the free energy barrier to increase to an unaffordably high limit.

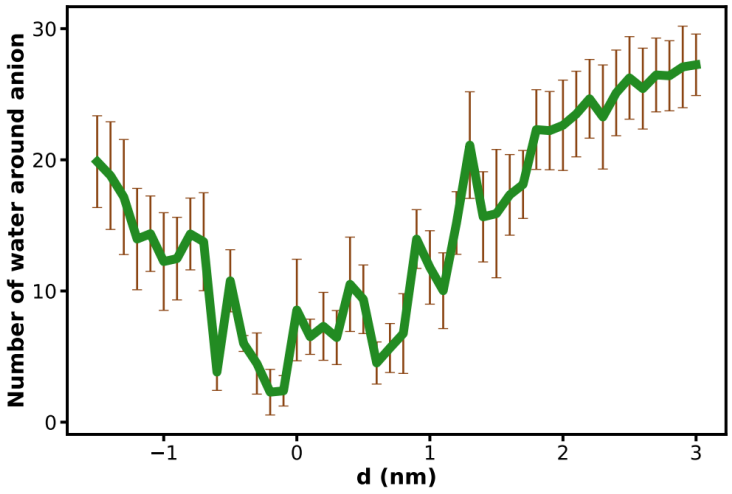

Fig. S22 Number of water molecules around the anion represented with the progression of the anion through the channel.

In the free energy curve, the presence of fine curvatures and also its periodic nature suggests considerable influence of channel chemical specificity on the ion transport energetics. Further, to gain the mechanistic insights of Cl^- ion transport and to understand how the transport process is sensitive to the chemical nature of the channel, the interactions which are key for the ion movement through the channel structure were characterized. Fig. S23 represents the number of contacts of the anion with the channel residues during its progression through the channel.

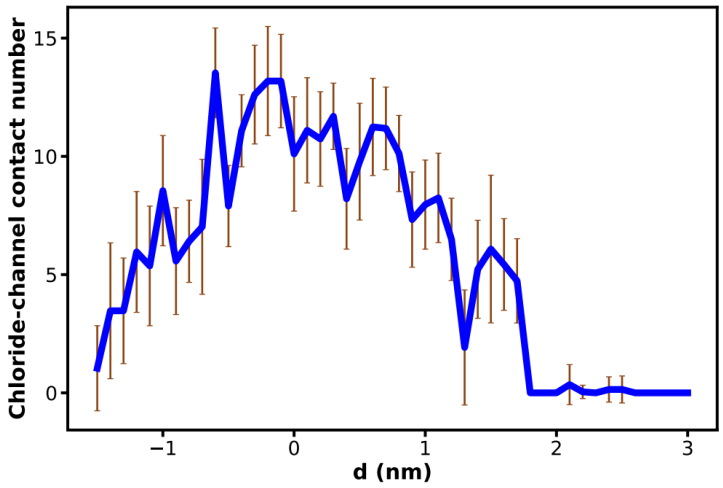

Fig. S23 The number of the contacts made by the chloride ion with the channel during its transport through the channel.

The contact of the Cl^- ion successively increases as the ion progresses through the channel and increases most as the ion resides at the central part of the channel. The Fig. S23 suggests that the anion moves through the channel by making its own contact with the channel. Fig. S24 depict the specific interaction of the channel residues with the passing anion. It is observed that the favourable interactions with the channel monomers with the anion makes the transport process easier.

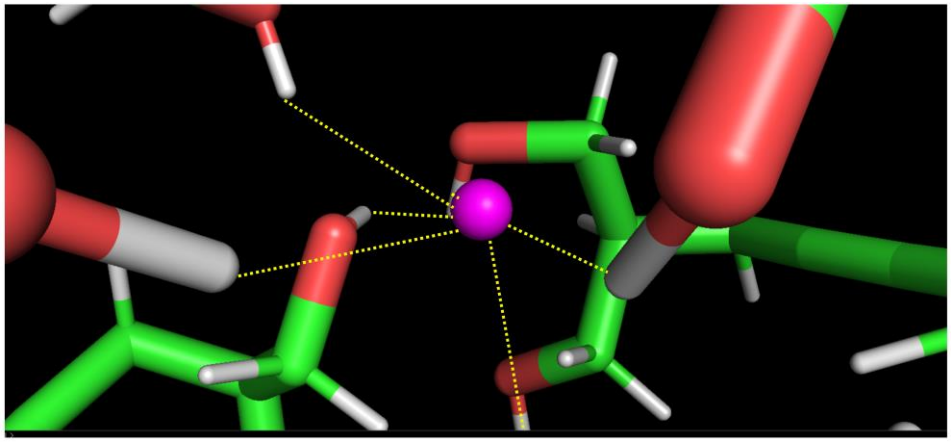

Fig. S24 The possible interactions between the chloride ion and the channel residues represented for the *trans* channel structure during ion progression.

X. NMR Spectra

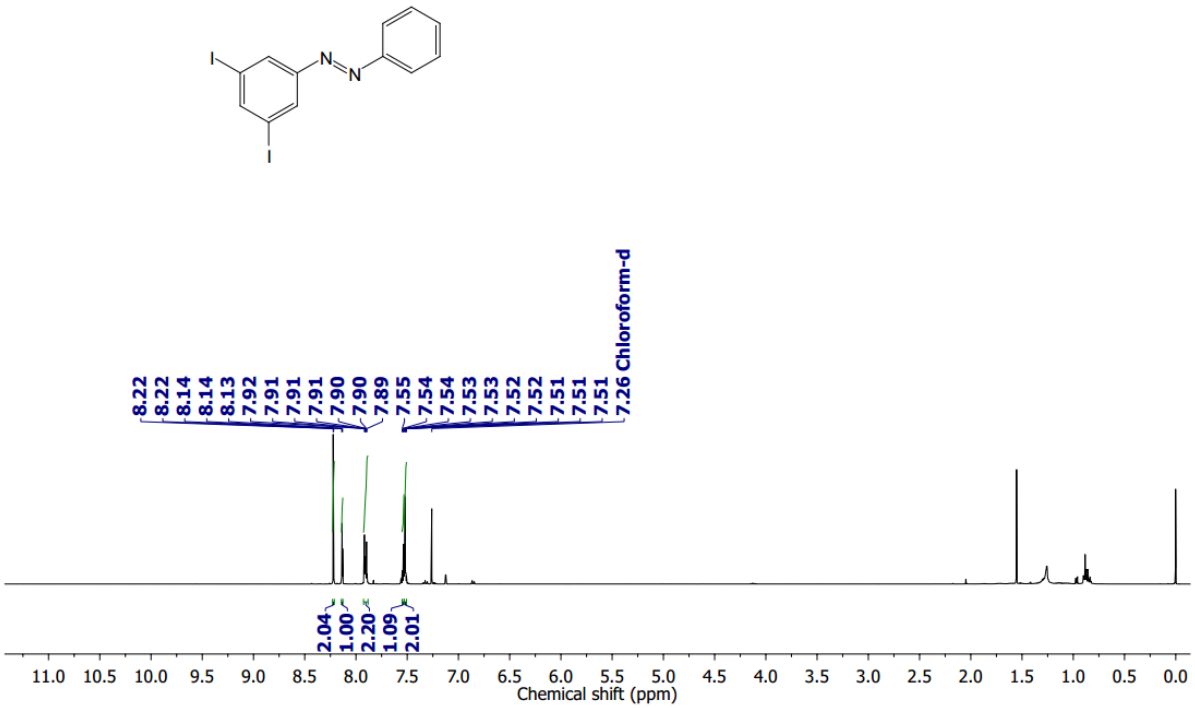

Fig. S25 ^{1}H NMR spectrum (400 MHz) of **4** in chloroform-*d* at room temperature.

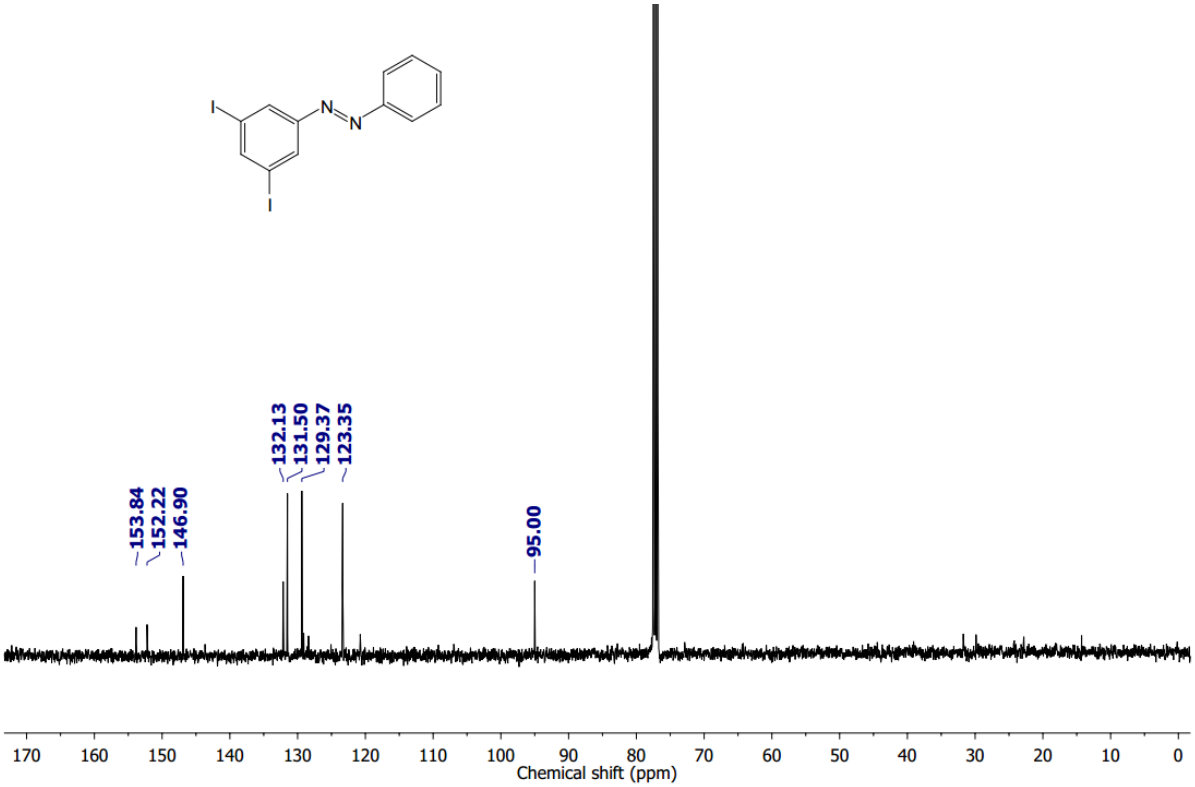

Fig. S26 ^{13}C NMR spectrum (101 MHz) of **4** in chloroform-*d* at room temperature.

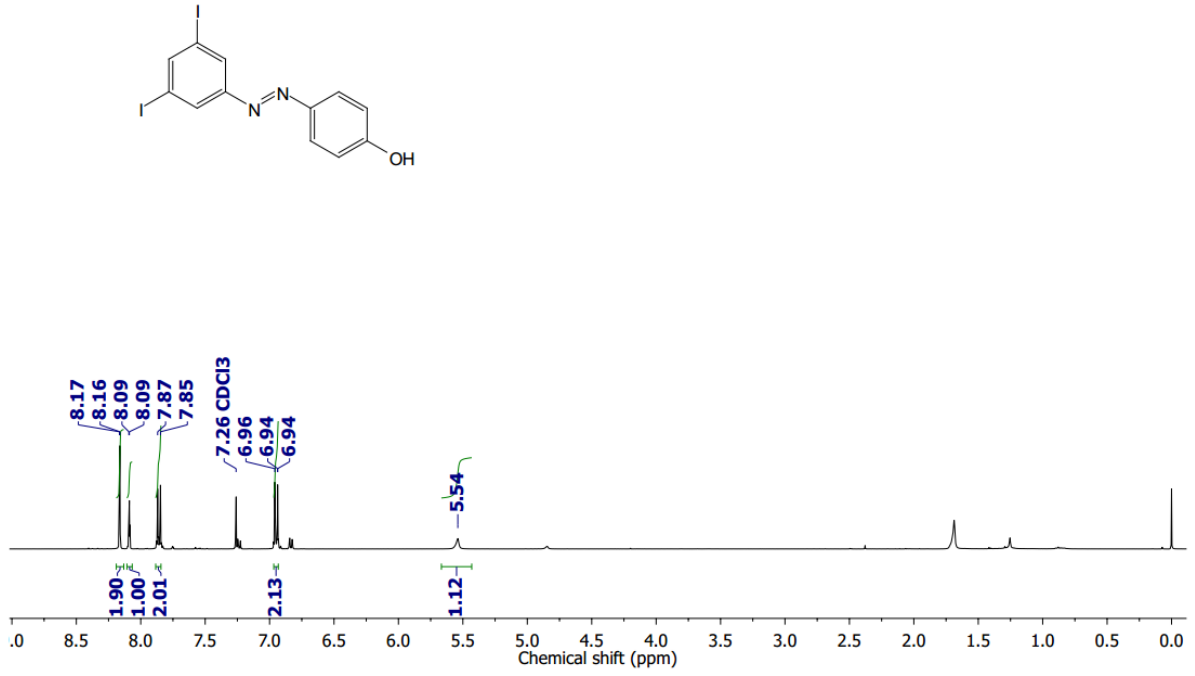

Fig. S27 ^{1}H NMR spectrum (400 MHz) of **6** in chloroform-*d* at room temperature.

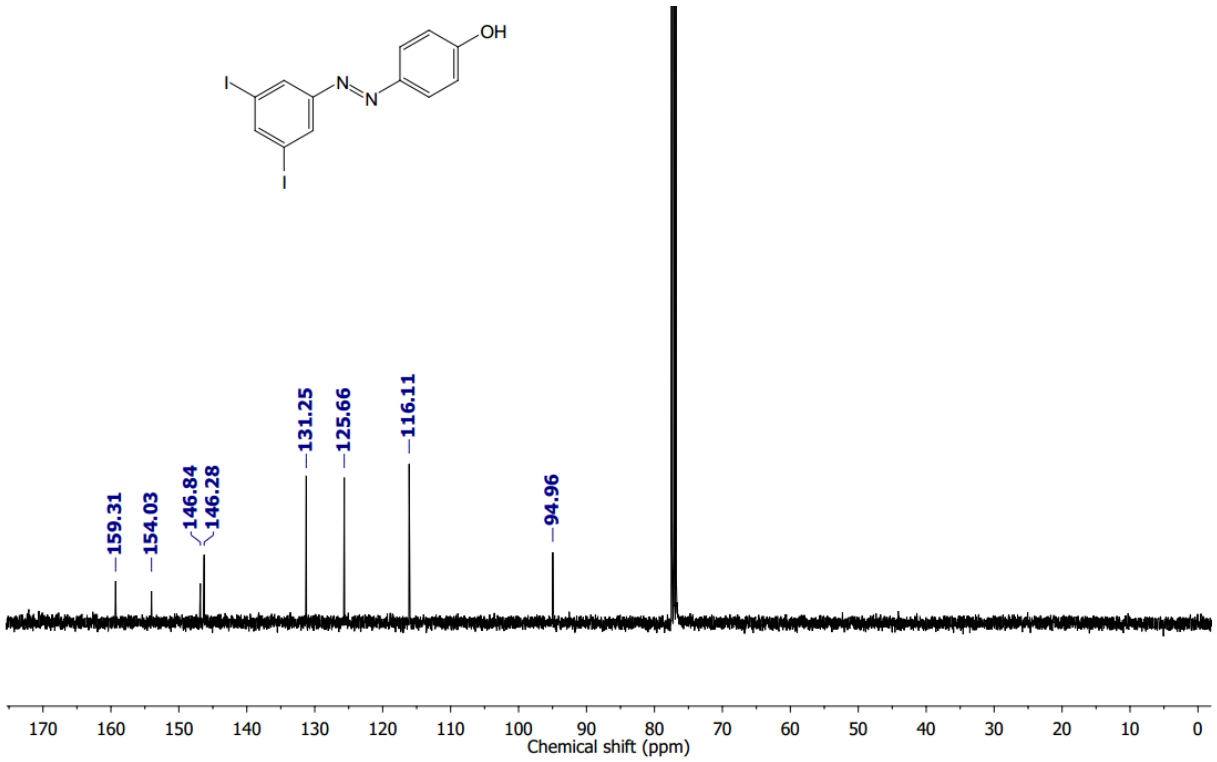

Fig. S28 ^{13}C NMR spectrum (101 MHz) of **6** in chloroform-*d* at room temperature.

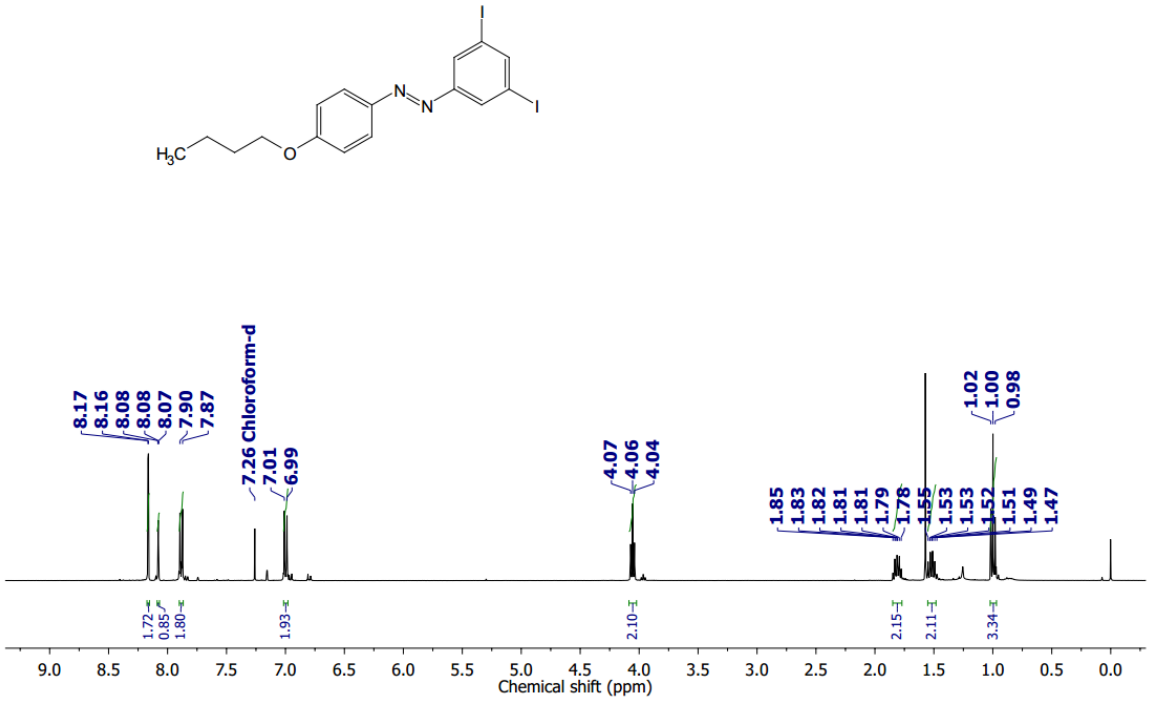

Fig. S29 ^{1}H NMR spectrum (400 MHz) of **7a** in chloroform-*d* at room temperature.

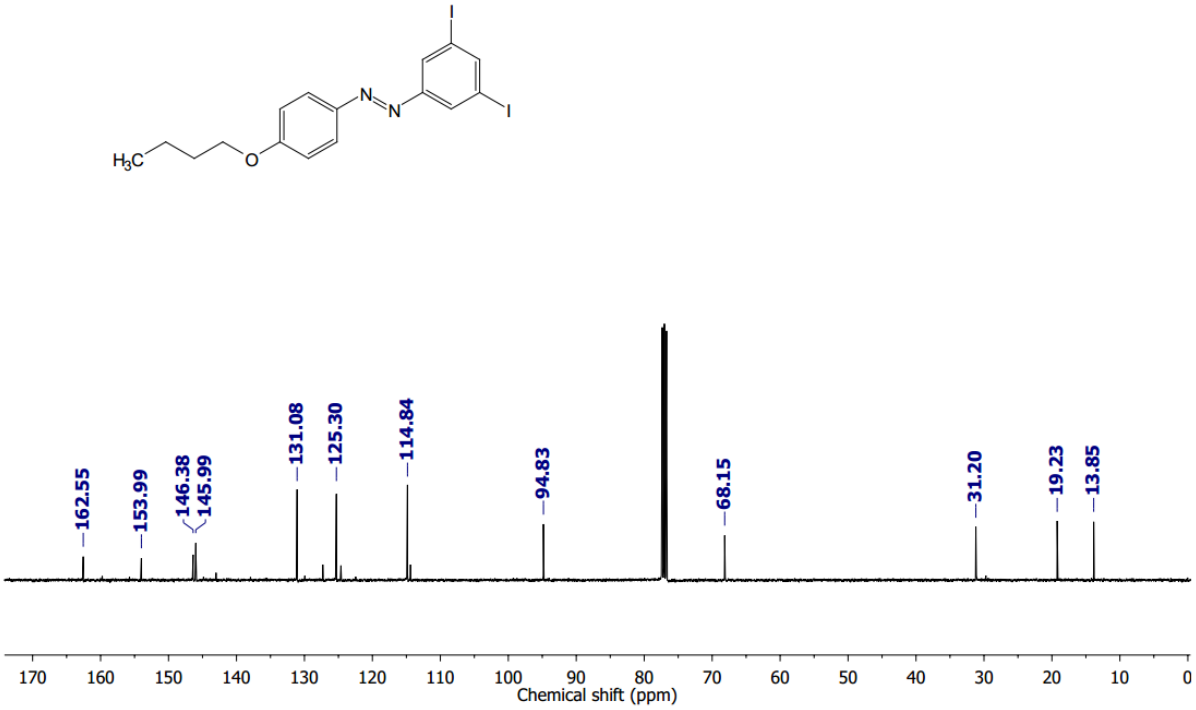

Fig. S30 ^{13}C NMR spectrum (101 MHz) of **7a** in chloroform-*d* at room temperature.

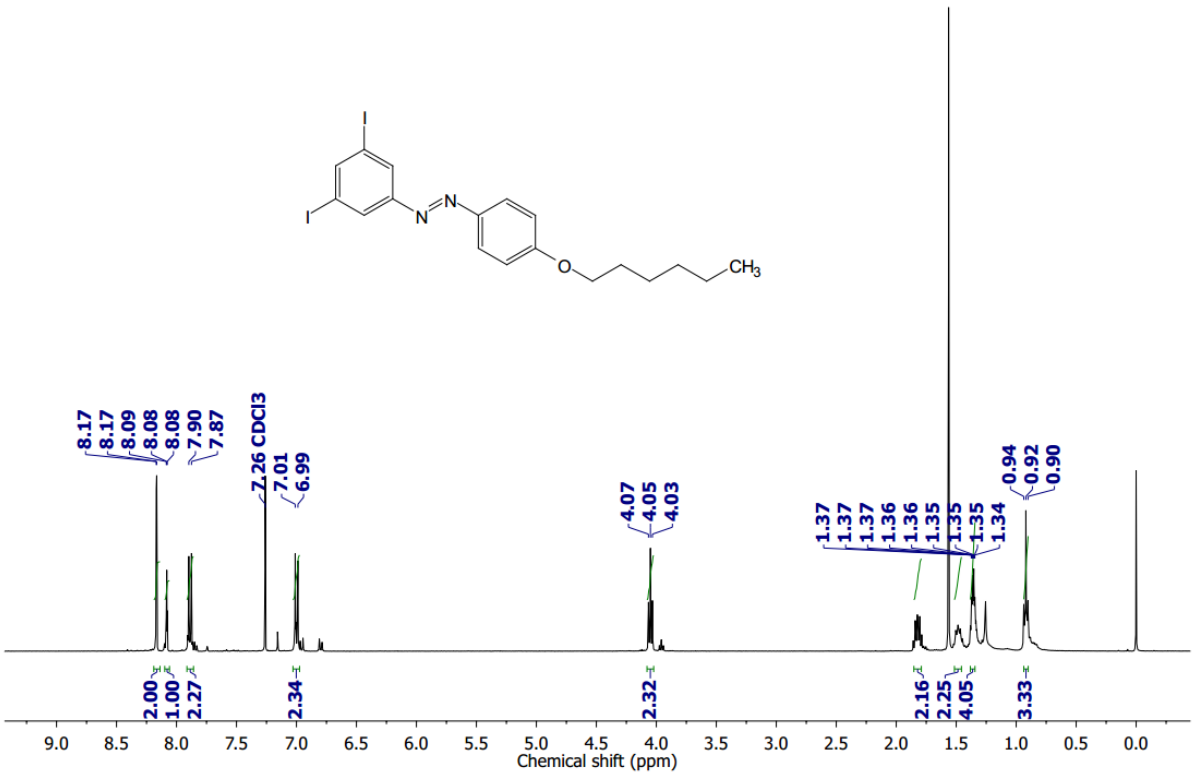

Fig. S31 ^{1}H NMR spectrum (400 MHz) of **7b** in chloroform-*d* at room temperature.

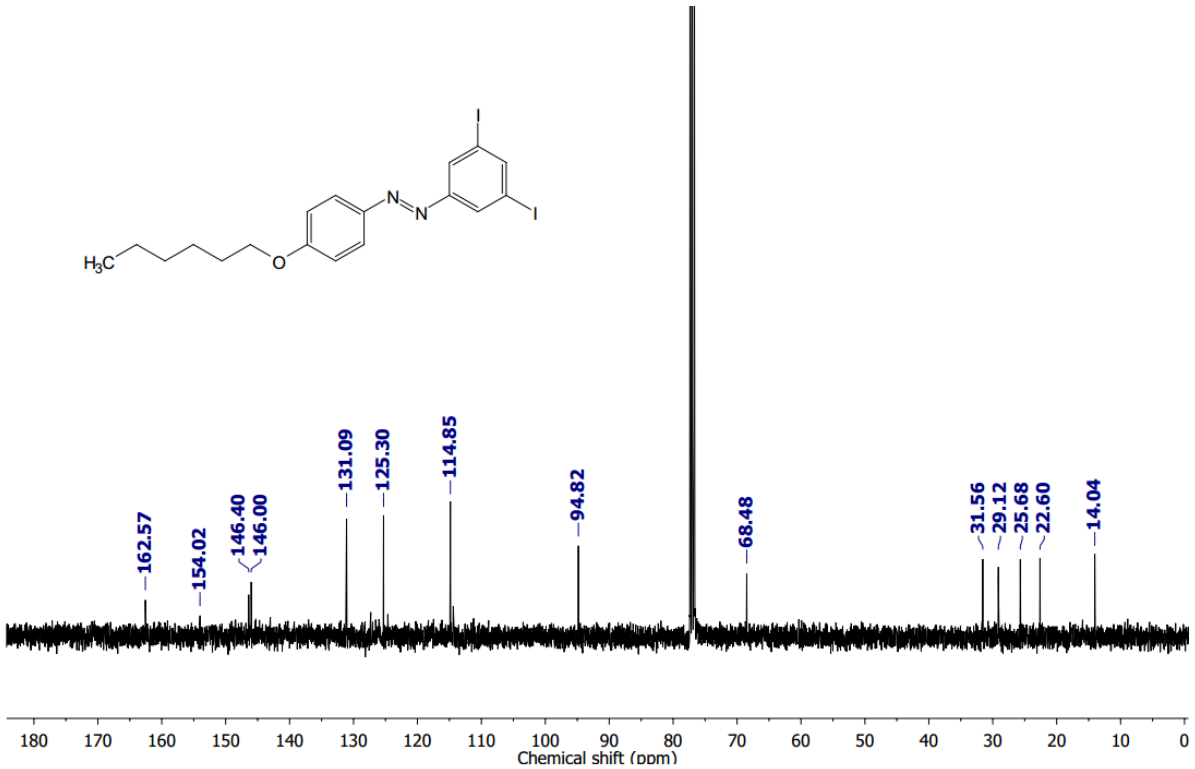

Fig. S32 ^{13}C NMR spectrum (101 MHz) of **7b** in chloroform-*d* at room temperature.

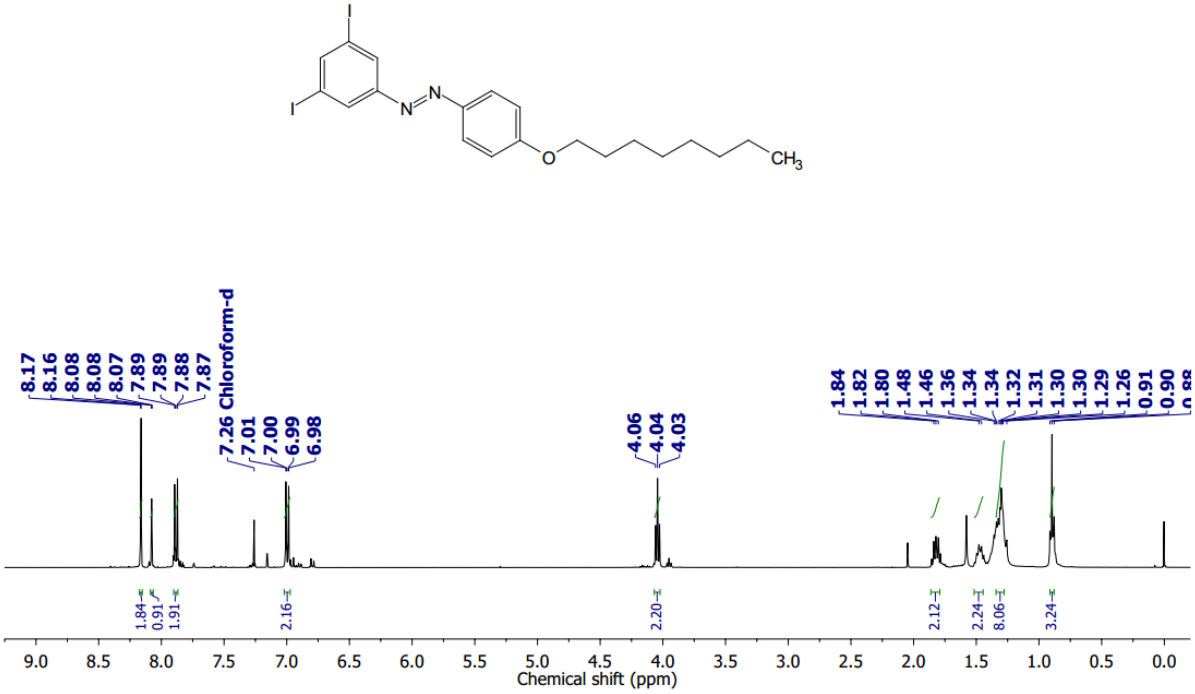

Fig. S33 ^{1}H NMR spectrum (400 MHz) of **7c** in chloroform-*d* at room temperature.

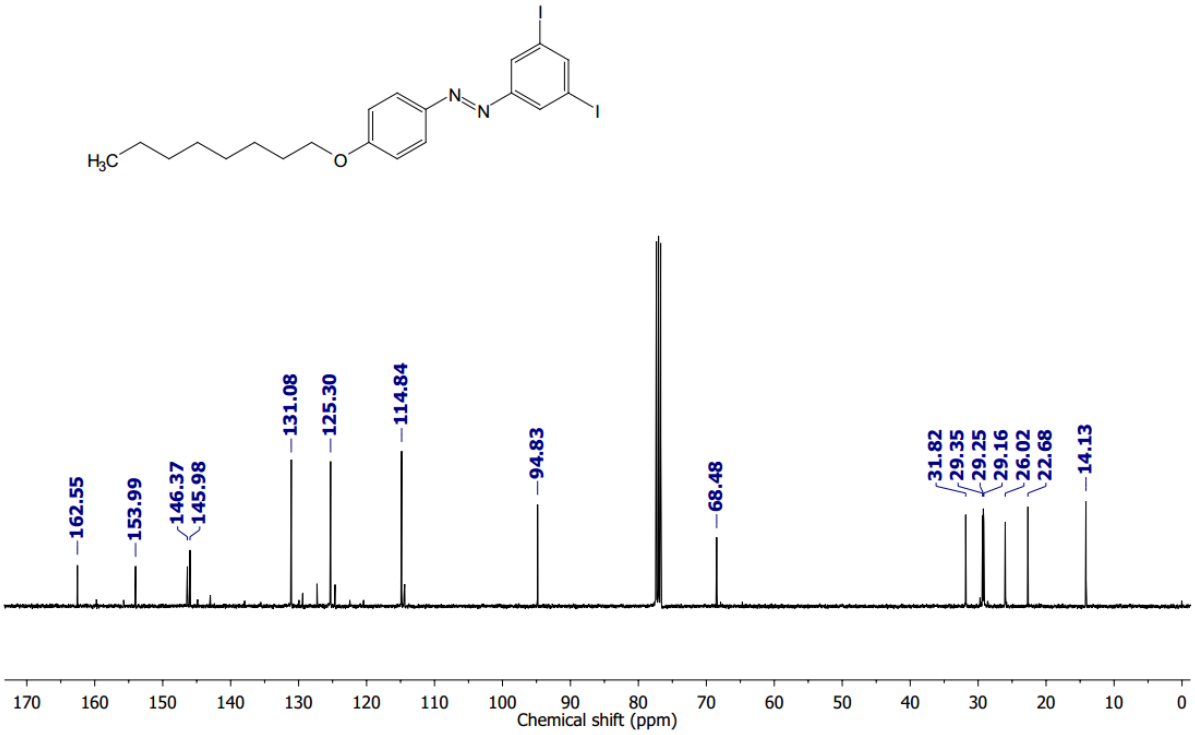

Fig. S34 ^{13}C NMR spectrum (101 MHz) of **7c** in chloroform-*d* at room temperature.

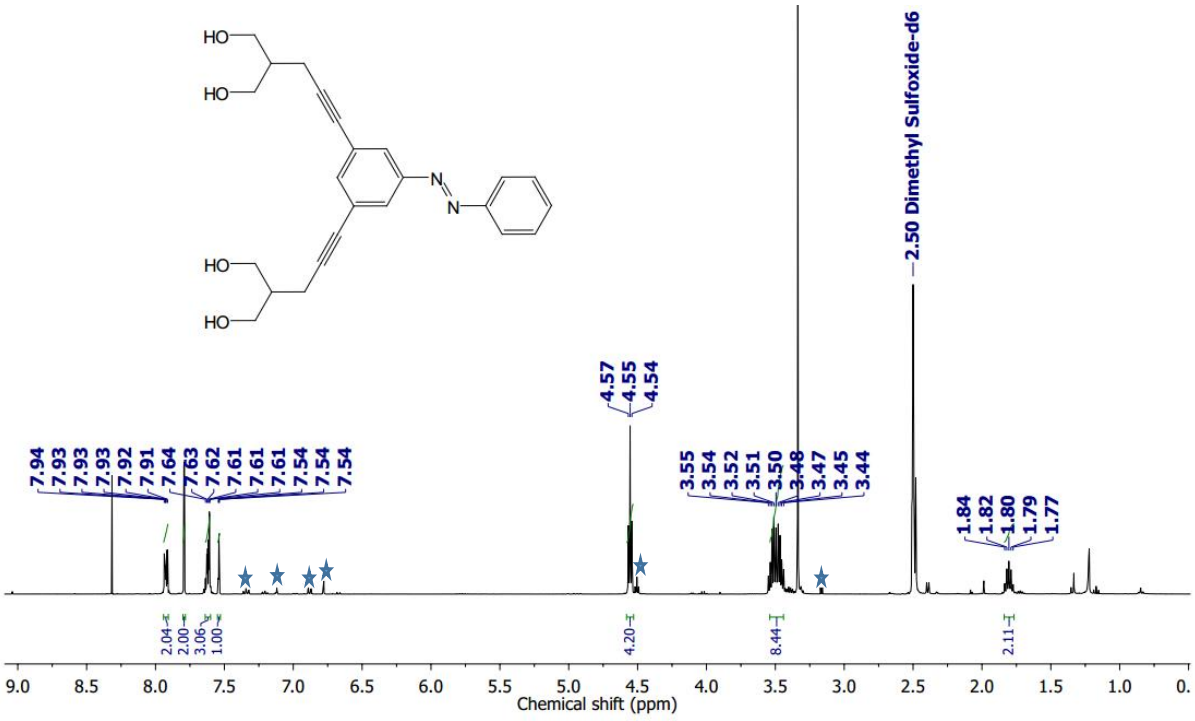

Fig. S35 ^{1}H NMR spectrum (400 MHz) of **1a** in DMSO-d_6 at room temperature. (★) is the presence of *cis* isomer.

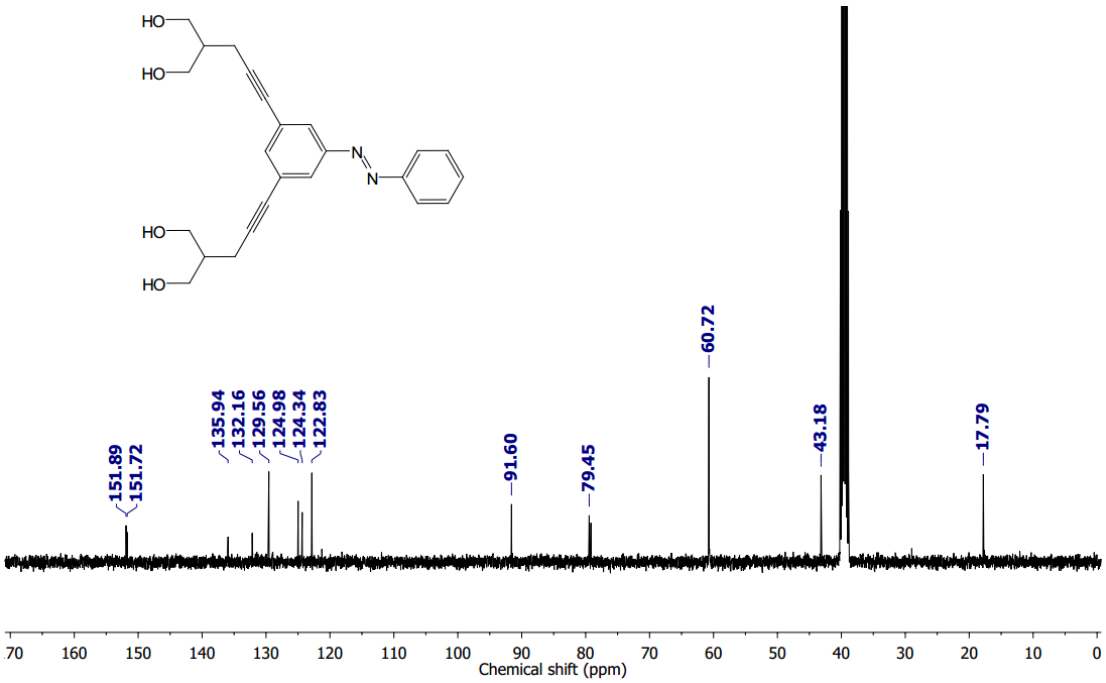

Fig. S36 ^{13}C NMR spectrum (101 MHz) of **1a** in DMSO-d_6 at room temperature. (★) is the presence of *cis* isomer.

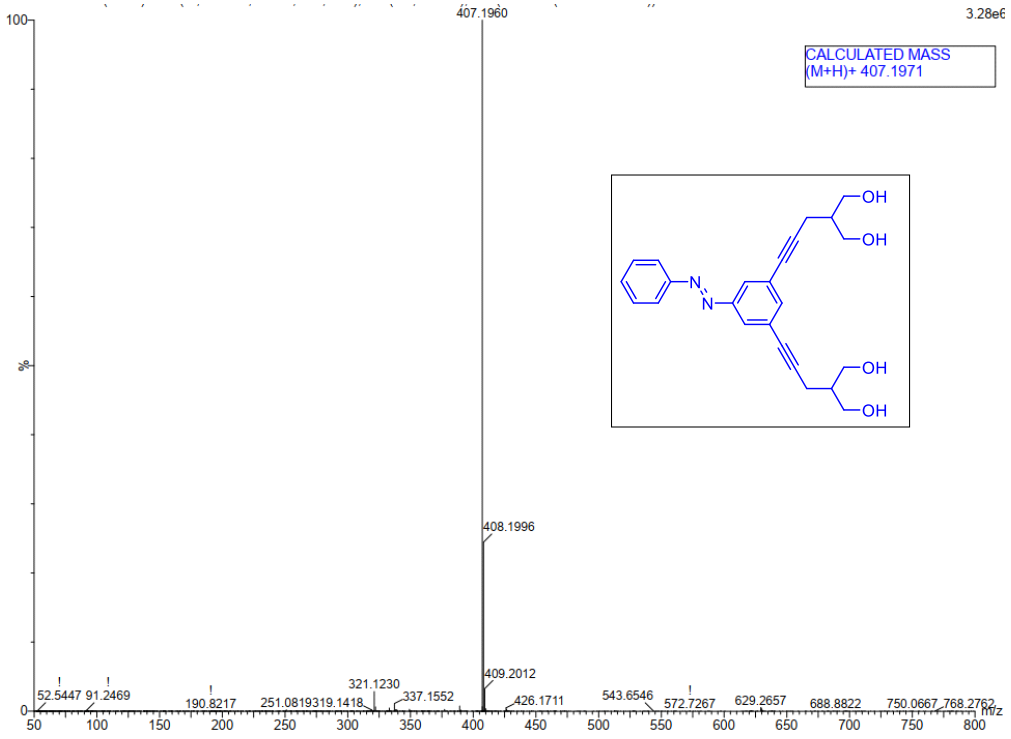

Fig. S37 ESI-MS spectrum of **1a** recorded in CH_3CN.

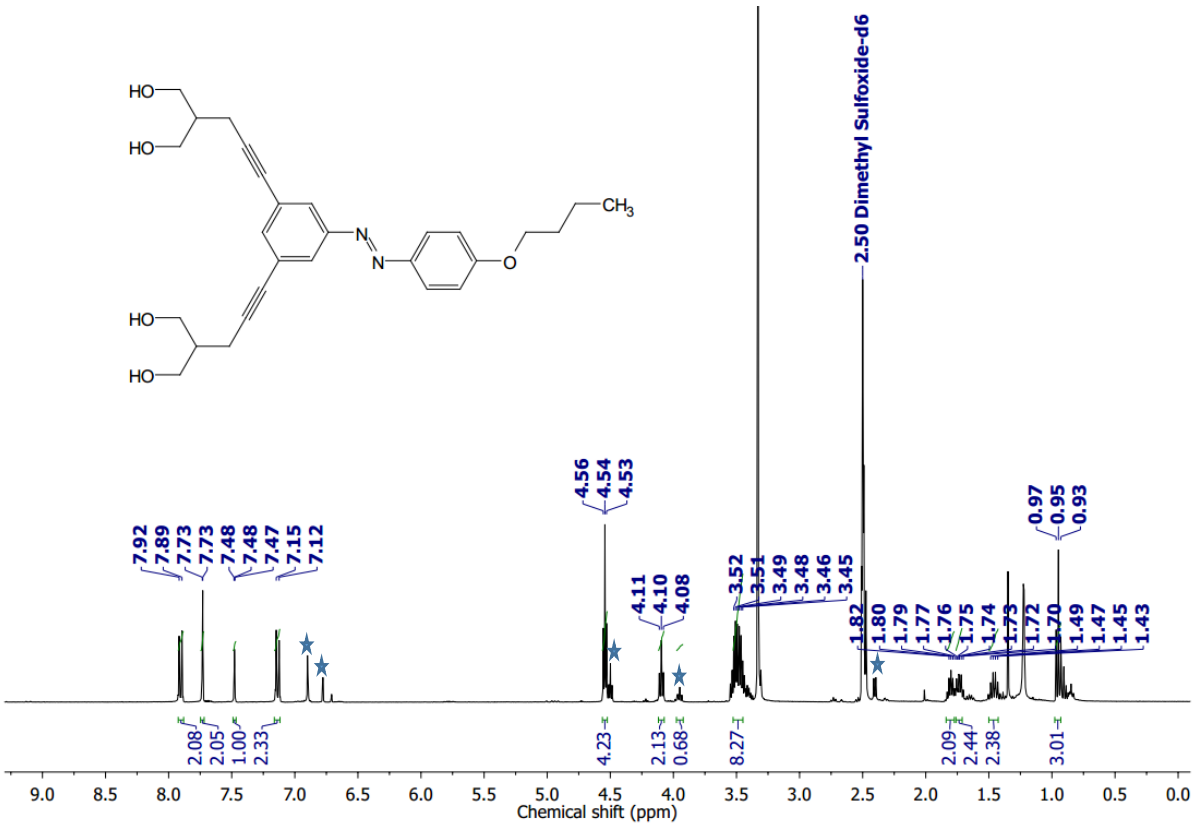

Fig. S38 ^{1}H NMR spectrum (101 MHz) of **1b** in DMSO-d_6 at room temperature. (★) is the presence of *cis* isomer.

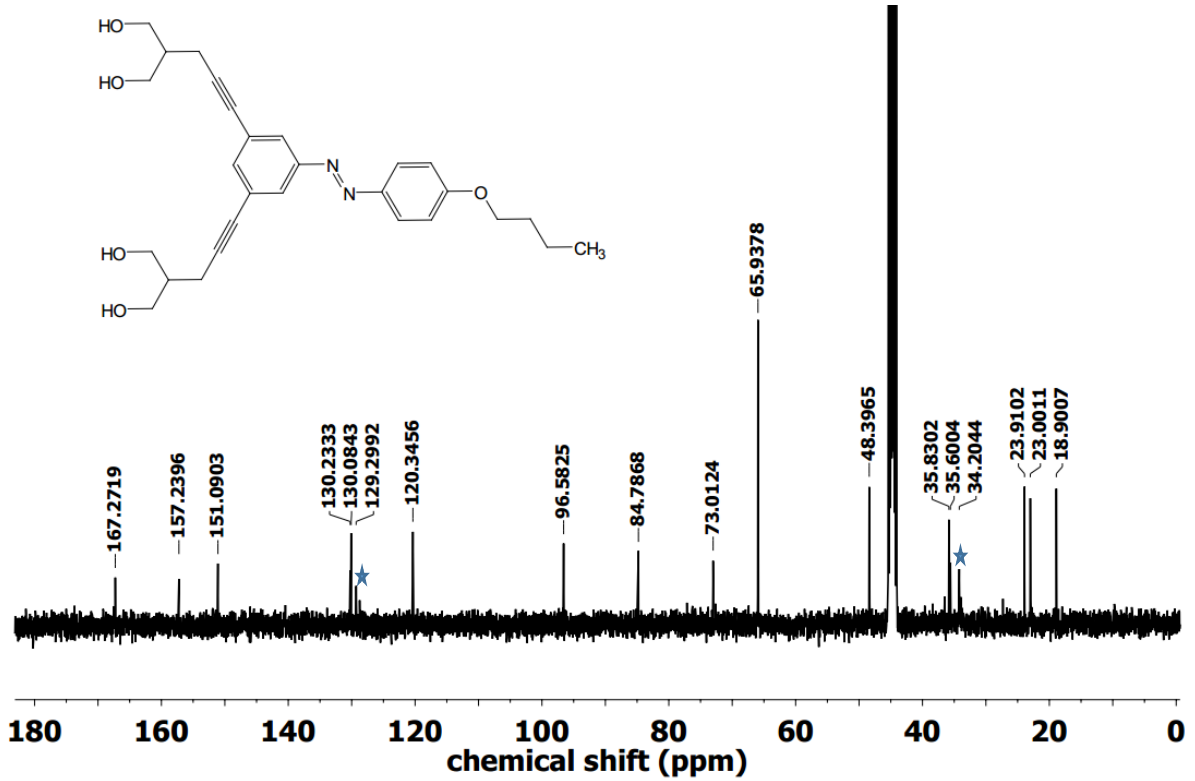

Fig. S39 101 MHz ^{13}C NMR spectrum of **1b** in DMSO-d_6. (★) is the presence of *cis* isomer.

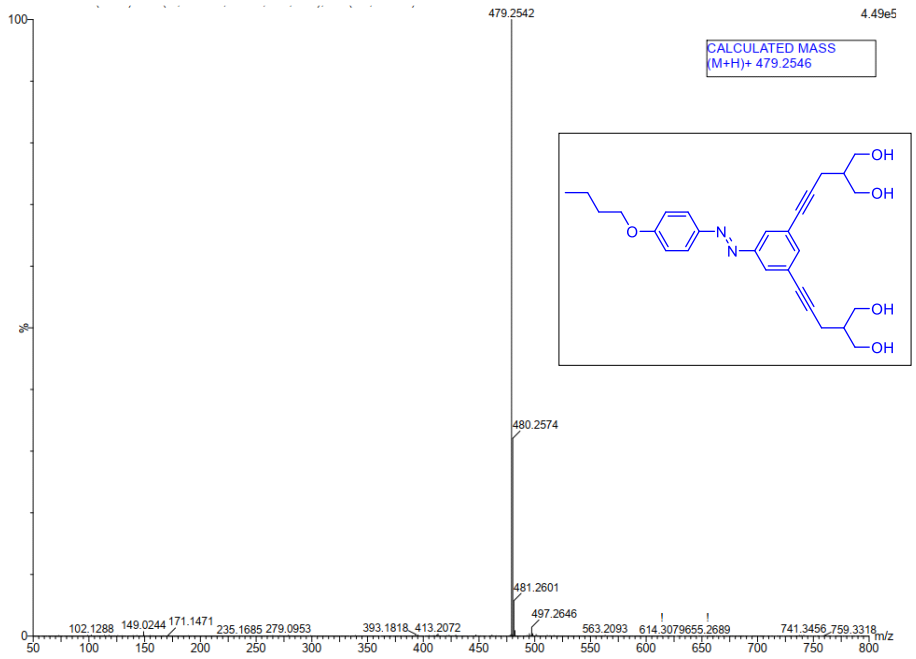

Fig. S40 ESI-MS spectrum of **1b** recorded in CH_3CN.

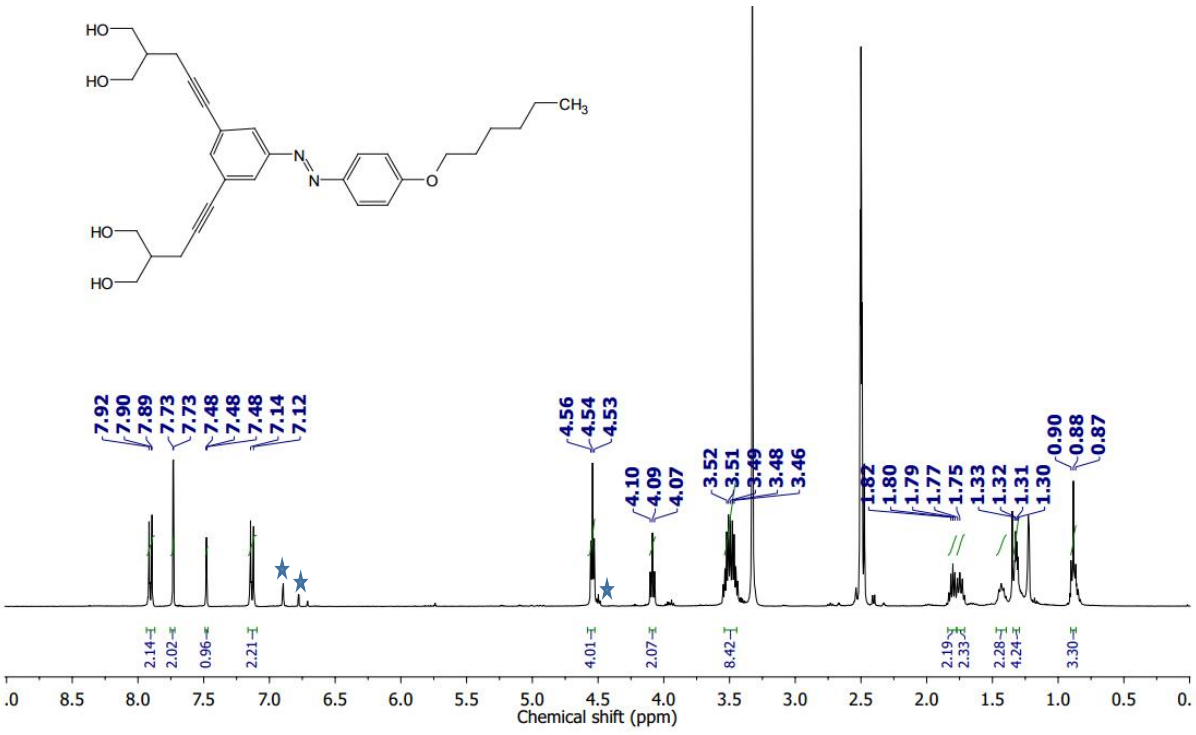

Fig. S41 400 MHz ^{1}H NMR spectrum of **1c** in DMSO-d_6. (★) is the presence of *cis* isomer.

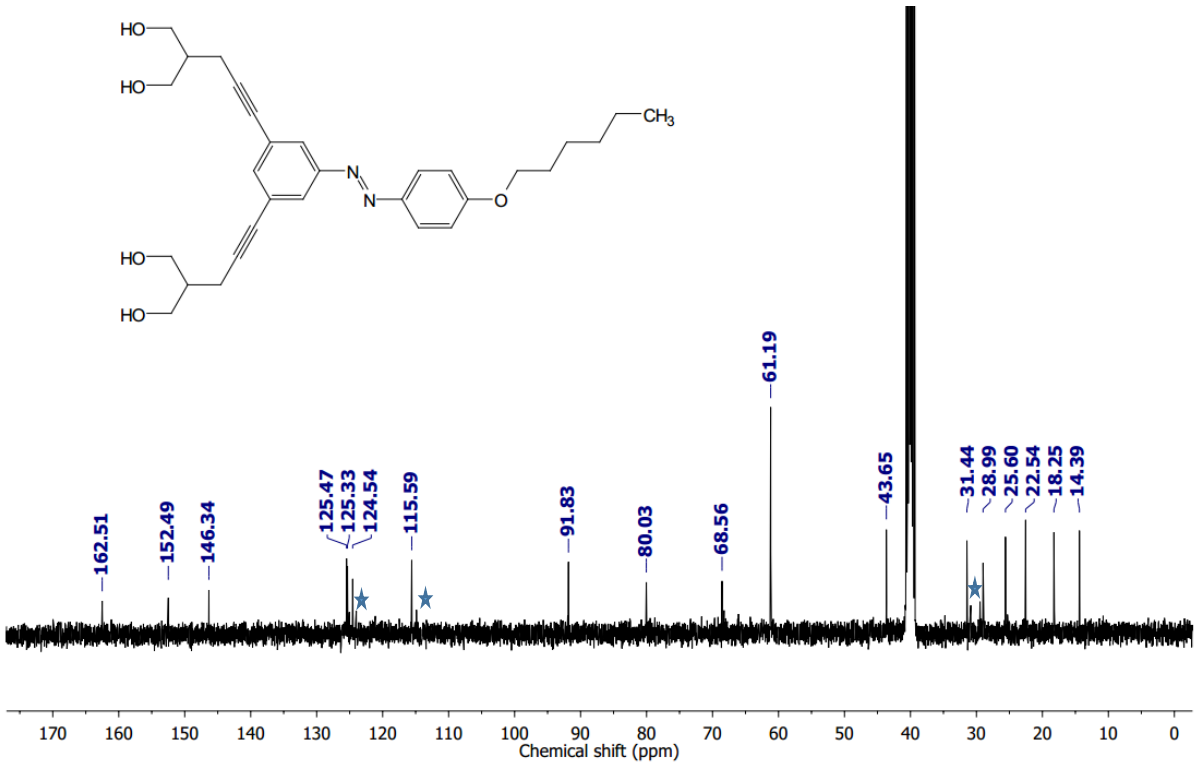

Fig. S42 101 MHz ^{13}C NMR spectrum of **1c** in DMSO-d_6. (★) is the presence of *cis* isomer.

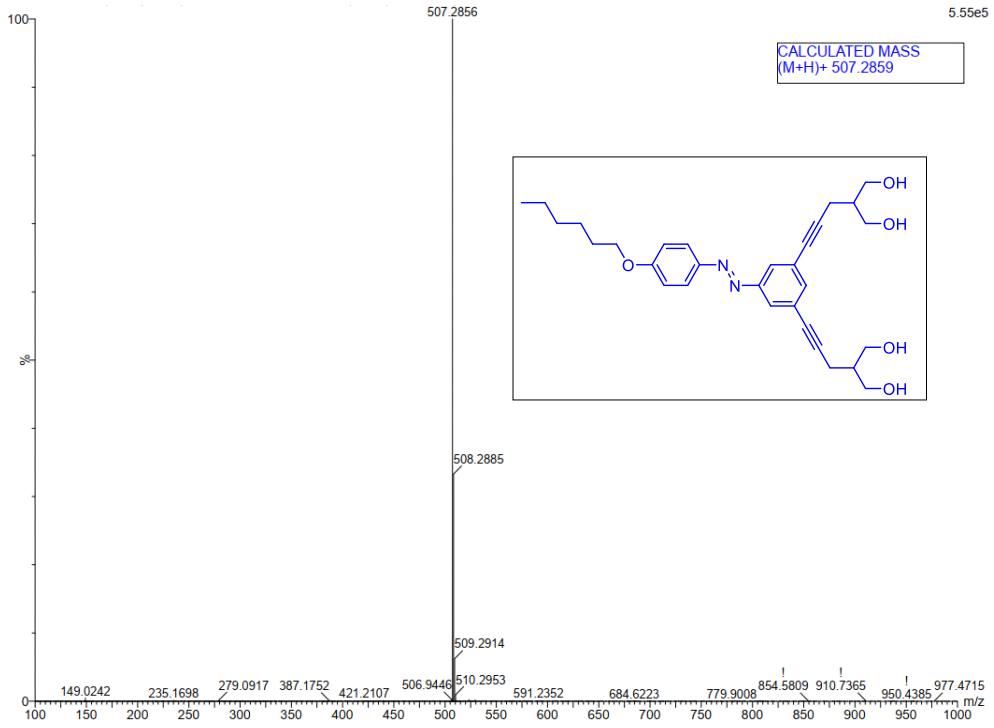

Fig. S43 ESI-MS spectrum of **1c** recorded in CH_3CN.

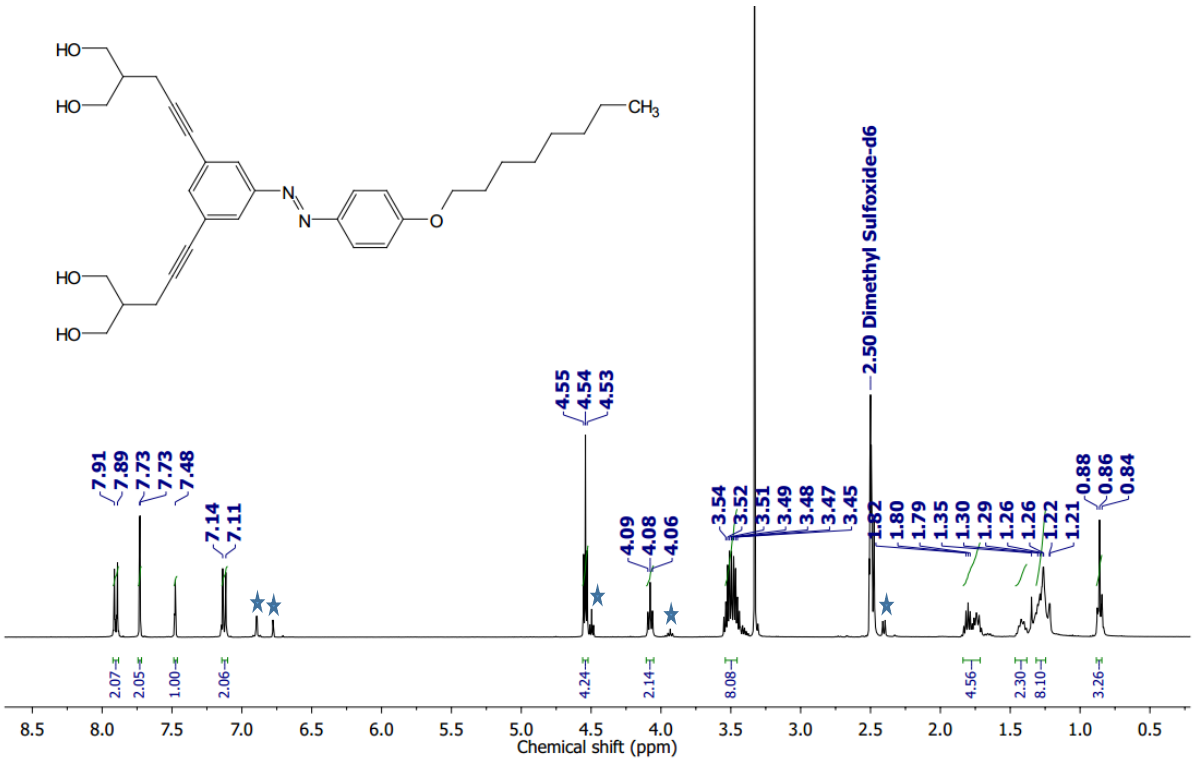

Fig. S44 400 MHz ^{1}H NMR spectrum of **1d** in DMSO-d_6. (★) is the presence of *cis* isomer.

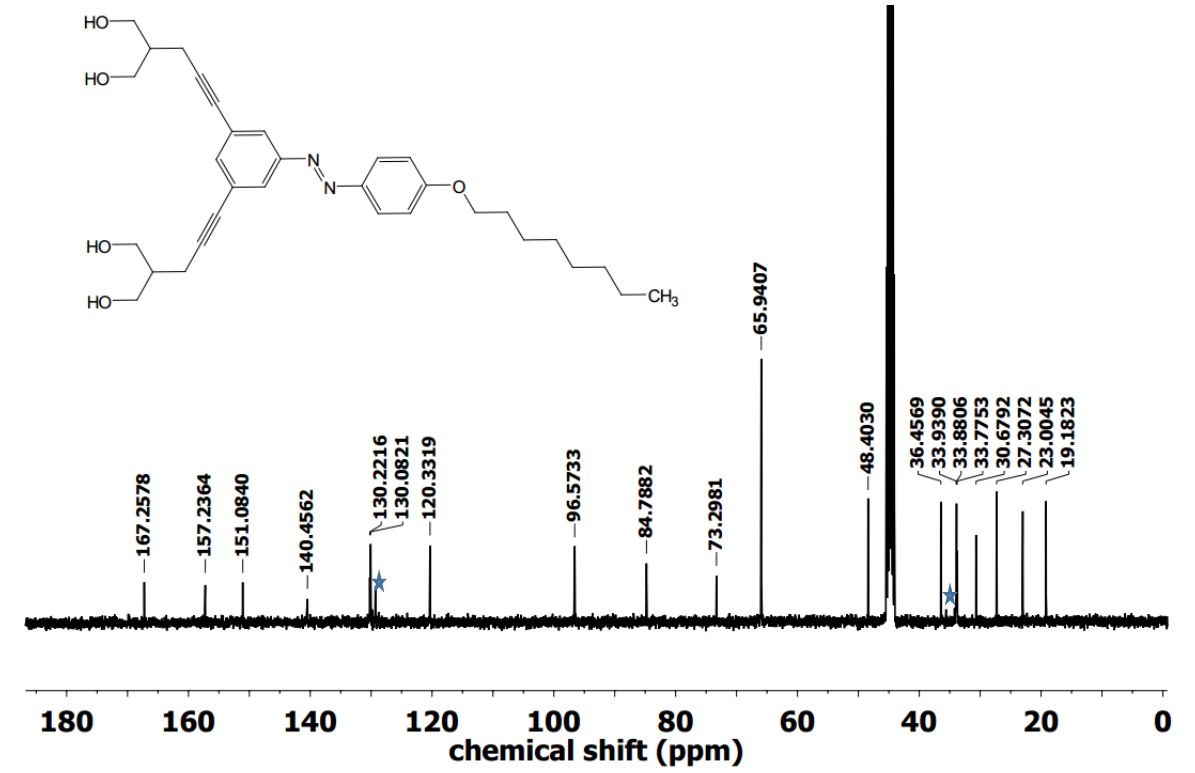

Fig. S45 101 MHz ^{13}C NMR spectrum of **1d** in DMSO-d_6. (★) is the presence of *cis* isomer.

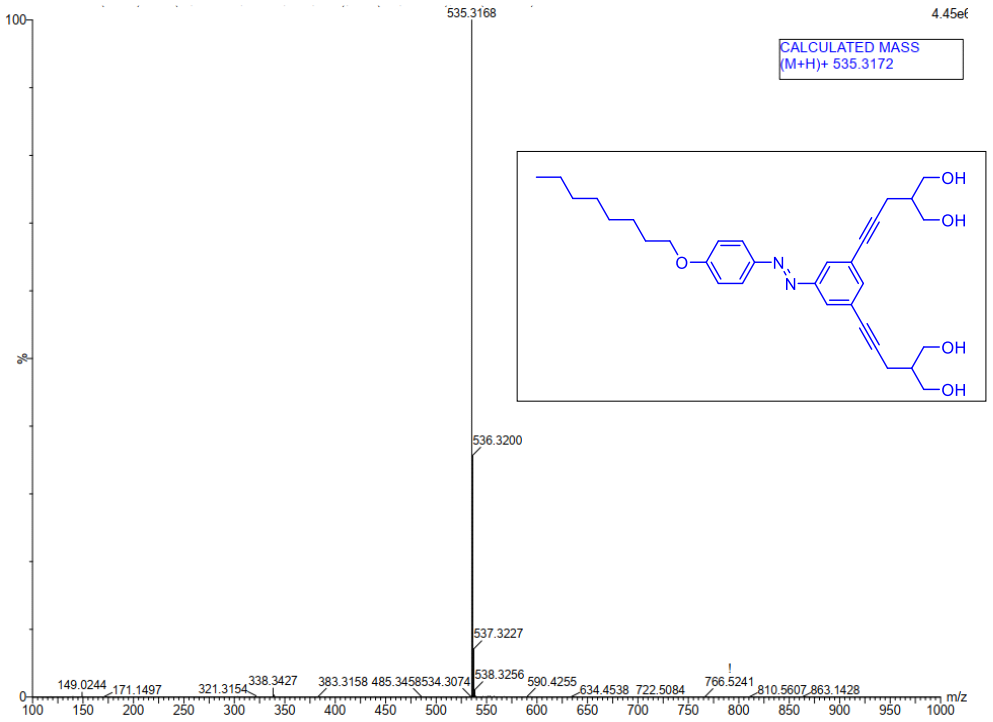

Fig. S46 ESI-MS spectrum of **1d** recorded in CH_3CN.

XI. References

S1. T. Saha, S. Dasari, D. Tewari, A. Prathap, K. M. Sureshan, A. K. Bera, A. Mukherjee and P. Talukdar, *J. Am. Chem. Soc.*, 2014, **136**, 14128-14135.

S2. P. Talukdar, G. Bollot, J. Mareda, N. Sakai and S. Matile, *J. Am. Chem. Soc.*, 2005, **127**, 6528-6529.

S3. V. Gorteau, G. Bollot, J. Mareda, A. Perez-Velasco and S. Matile, *J. Am. Chem. Soc.*, 2006, **128**, 14788-14789.

S4. A. V. Jentzsch and S. Matile, *J. Am. Chem. Soc.*, 2013, **135**, 5302-5303.

S5. S. Bhosale and S. Matile, *Chirality*, 2006, **18**, 849-856.

S6. C. Ren, X. Ding, A. Roy, J. Shen, S. Zhou, F. Chen, S. F. Yau Li, H. Ren, Y. Y. Yang and H. Zeng, *Chem. Sci.*, 2018, **9**, 4044-4051.

S7. D. Mondal, A. Sathyan, S. V. Shinde, K. K. Mishra and P. Talukdar, *Org. Biomol. Chem.*, 2018, **16**, 8690-8694.

S8. B. Hille, *Ion Channels of Excitable Membranes, 3rd Edition*, 2001, **Sinauer**.

S9. O. S. Smart, J. Breed, G. R. Smith and M. S. Sansom, *Biophys J*, 1997, **72**, 1109-1126.

S10. D. Dash, S. Kumar, C. Mallika and U. K. Mudali, *Int. Sch. Res. Net.*, 2012, **2012**, 730154.

S11. N. Schrödinger Release 2022-1: Maestro; Schrödinger LLC: New York, USA, 2021.

S12. S. Jo, T. Kim, V. G. Iyer and W. Im, *J. Comput. Chem*, 2008, **29**, 1859-1865.

S13. S. Jo, J. B. Lim, J. B. Klauda and W. Im, *Biophys. J.*, 2009, **97**, 50-58.

S14. K. G. Sprenger, V. W. Jaeger and J. Pfaendtner, *J. Phys. Chem. B*, 2015, **119**, 5882-5895.

S15. B. R. Brooks, C. L. B. Iii, A. D. Mackerell Jr, L. Nilsson, R. J. Petrella, B. Roux, Y. Won, G. Archontis, C. Bartels, S. Boresch, A. Caflisch, L. Caves, Q. Cui, A. R. Dinner,

M. Feig, S. Fischer, J. Gao, M. Hodoscek, W. Im, K. Kuczera, T. Lazaridis, J. Ma, V. Ovchinnikov, E. Paci, R. W. Pastor, C. B. Post, J. Z. Pu, M. Schaefer, B. Tidor, R. M. Venable, H. L. Woodcock, X. Wu, W. Yang, D. M. York and M. Karplus, *J. Comput. Chem.*, 2009, **30**, 1545-1614.

S16. J. Huang, S. Rauscher, G. Nawrocki, T. Ran, M. Feig, B. L. de Groot, H. Grubmüller and A. D. MacKerell, *Nat. Methods*, 2017, **14**, 71-73.

S17. W. L. Jorgensen, J. Chandrasekhar, J. D. Madura, R. W. Impey and M. L. Klein, *J. Chem. Phys.*, 1983, **79**, 926-935.

S18. T. Darden, D. York and L. Pedersen, *J. Chem. Phys.*, 1993, **98**, 10089-10092.

S19. B. Hess, H. Bekker, H. J. C. Berendsen and J. G. E. M. Fraaije, *J. Comput. Chem.*, 1997, **18**, 1463-1472.

S20. S. Miyamoto and P. A. Kollman, *J. Comput. Chem.*, 1992, **13**, 952-962.

S21. S. Páll and B. Hess, *Comput. Phys. Commun.*, 2013, **184**, 2641-2650.

S22. H. J. C. Berendsen, J. P. M. Postma, W. F. van Gunsteren, A. DiNola and J. R. Haak, *J. Chem. Phys.*, 1984, **81**, 3684-3690.

S23. D. J. Evans and B. L. Holian, *J. Chem. Phys.*, 1985, **83**, 4069-4074.

S24. M. Parrinello and A. Rahman, *J. Chem. Phys.*, 1981, **52**, 7182-7190.